catalysts

MDPI

Article

$BiPO_4$/Ov-BiOBr High-Low Junctions for Efficient Visible Light Photocatalytic Performance for Tetracycline Degradation and H_2O_2 Production

Minghui Tang [1], Xibao Li [1,2,*], Fang Deng [2], Lu Han [3], Yu Xie [2], Juntong Huang [1], Zhi Chen [1], Zhijun Feng [1] and Yingtang Zhou [4,*]

1 School of Materials Science and Engineering, Nanchang Hangkong University, Nanchang 330063, China
2 National-Local Joint Engineering Research Center of Heavy Metal Pollutants Control and Resource Utilization, Nanchang Hangkong University, Nanchang 330063, China
3 School of Materials and Metallurgy, University of Science and Technology Liaoning, Anshan 114051, China
4 National Engineering Research Center for Marine Aquaculture, Marine Science and Technology College, Zhejiang Ocean University, Zhoushan 316004, China
* Correspondence: lixibao@nchu.edu.cn (X.L.); zhouyingtang@zjou.edu.cn (Y.Z.)

Abstract: Through a two-step solvothermal method, different molar ratios of $BiPO_4$ were grown in situ on the surface of oxygen-vacancy-rich BiOBr (Ov-BiOBr), successfully constructing a $BiPO_4$/Ov-BiOBr heterojunction composite material. By constructing a novel type I high-low junction between the semiconductor $BiPO_4$ and Ov-BiOBr, stronger oxidative holes or reductive electrons were retained, thereby improving the redox performance of the photocatalyst. The composite catalyst with a 10% molar content of $BiPO_4$ demonstrated the highest degradation rate of tetracycline (TC), degrading over 95% within 90 min, with a rate constant of 0.02534 min^{-1}, which is 2.3 times that of Ov-BiOBr and 22 times that of $BiPO_4$. The 10% $BiPO_4$/Ov-BiOBr sample displayed the best photocatalytic activity, producing 139 $\mu mol \cdot L^{-1}$ H_2O_2 in 120 min, which is 3.6 times the efficiency of Ov-BiOBr and 19 times that of $BiPO_4$. This was due to the appropriate bandgap matching between $BiPO_4$ and Ov-BiOBr, the photo-generated electron transfer channel via Bi-bridge, and efficient charge separation. It was inferred that the free radical species ·OH and $\cdot O_2^-$ played the dominant role in the photocatalytic process. Based on experimental and theoretical results, a possible photocatalytic mechanism was proposed.

Keywords: $BiPO_4$; BiOBr; oxygen vacancy; high-low junction; photocatalysis

check for updates

Citation: Tang, M.; Li, X.; Deng, F.; Han, L.; Xie, Y.; Huang, J.; Chen, Z.; Feng, Z.; Zhou, Y. $BiPO_4$/Ov-BiOBr High-Low Junctions for Efficient Visible Light Photocatalytic Performance for Tetracycline Degradation and H_2O_2 Production. *Catalysts* **2023**, *13*, 634. https://doi.org/10.3390/catal13030634

Academic Editor: Xiaowang Lu

Received: 4 March 2023
Revised: 19 March 2023
Accepted: 20 March 2023
Published: 22 March 2023

1. Introduction

Since the acceleration of urbanization and rapid industrial development in modern times, environmental pollution has created increasingly serious problems, among which organic pollution has gradually become one of the major issues faced by human society in the 21st century. Tetracycline (TC), a widely used antibiotic, is present in numerous wastewater streams and environmental samples. Its excessive use and discharge have led to environmental pollution issues, such as the spread of antibiotic resistance genes. Therefore, studying the photocatalytic degradation of tetracycline is of significant environmental importance. As a pollutant with representative antibiotic structural features, tetracycline's photocatalytic degradation helps in better understanding and evaluating the treatment effects of different photocatalysts on similar contaminants. The high stability and low natural degradation of tetracycline in water present challenges for the design and optimization of photocatalysts. The aim is to discover novel and efficient photocatalysts through the study of tetracycline's photocatalytic degradation process. Various methods have been employed for tetracycline degradation, including biodegradation, photochemical degradation, advanced oxidation processes (AOPs), membrane filtration technology and

adsorption. However, these methods have drawbacks such as slow degradation rates, high energy consumption, susceptibility to environmental conditions, generation of secondary pollutants, stringent operating conditions, only achieving separation and concentration rather than true degradation of pollutants, reaching adsorption saturation easily, and the potential for membrane fouling. The photocatalytic method is chosen for tetracycline degradation in this research due to its environmental friendliness, low energy consumption, and lack of secondary pollution. By designing and optimizing photocatalysts, the goal is to improve degradation efficiency and reduce energy consumption. In terms of environmental purification, semiconductor catalysis technology has become a promising green energy utilization technology, which has significant advantages over traditional organic treatment methods, such as no secondary pollution, low cost, and strong oxidation, and has received widespread attention. The research focus of photocatalytic semiconductor catalysis technology is the selection, synthesis, and performance improvement of semiconductors [1–4].

The photocatalytic performance of heterojunctions mainly depends on the generation of electron-hole pairs in the conduction and valence bands after absorbing light energy and maintaining spatial separation to participate in redox reactions, thus achieving photocatalytic effects [5–7]. However, due to the structural characteristics of the semiconductor material itself, the recombination rate of photo-generated charge carriers is usually greater than the migration rate. In addition, the bandgap width of the semiconductor material itself is too large, and the wavelength range of light absorption is too narrow, resulting in a decrease in the absorption and utilization efficiency of visible light, which leads to the excited electrons and holes not being able to participate in redox reactions in a timely manner; instead, they are lost in the form of thermal energy or light energy [8]. Therefore, the recombination of electron-hole pairs and the wavelength range of light absorption by semiconductor materials are the two main factors affecting the photocatalytic performance of composite photocatalysts [9,10].

BiOBr is a ternary bismuth-based layered semiconductor photocatalyst. The staggered arrangement of its layered structure leads to an inherent electric field between the Br- layer and the $[Bi_2O_2]^{2+}$ layer, facilitating better separation of electrons and holes [11–14]. Moreover, BiOBr has oxygen vacancy defect sites, which can capture excited-state electrons and create spatial separation between different photogenerated charge carriers, preventing recombination and improving the efficiency of redox reactions. The layered structure of BiOBr can effectively reduce the probability of recombination of photogenerated charge carriers; moreover, BiOBr has good electrical, optical, and magnetic properties. Density functional theory calculations show that under illumination, electrons in Br 4p of BiOBr are excited and pass through the K layer to reach the conduction band, making it difficult for holes and electrons to recombine. Wu et al. prepared a new photocatalyst, p-n heterojunction $BiOBr/La_2Ti_2O_7$, and used in situ FT-IR dynamic monitoring of the adsorption-reaction process of visible light oxidation of NO [15]. They found that the built-in electric field could accelerate the separation of e^--h^+ pairs, thus improving the photocatalytic efficiency. In addition, Ye et al. anchored Fe^{3+} sites on oxygen-deficient BiOBr nanosheets, effectively regulating charge/energy transfer and adsorption of reactants, thereby enhancing the dual functions of photocatalytic reaction and highly selective activation of O_2 to $^1O_2$ [16]. $BiPO_4$ is an n-type semiconductor with three crystal structures: low-temperature monoclinic phase, high-temperature monoclinic phase, and hexagonal phase. The low-temperature monoclinic phase has the highest photocatalytic efficiency, especially when combined with a staggered heterojunction formed with BiOBr, which promotes the separation of electron-hole pairs. Despite its small bandgap width of only 3.8–4.2 eV, $BiPO_4$ has a narrow absorption range and can only absorb UV light [17,18]. However, $BiPO_4$ contains the non-metallic oxide PO_4^{3-}, which induces the separation of photoinduced electron-hole pairs and the abundance of negatively charged PO_4^{3-} facilitates this separation, thereby enhancing photocatalytic activity [19]. $BiPO_4$ nanoparticles are actually aggregates of $BiPO_4$ quantum dots with an average diameter of about 5 nm [20]. Therefore, ultrathin

Bi nanosheets can increase edge sites and promote the conversion of CO_2 to carboxylates, increasing the redox reaction sites and improving photocatalytic efficiency. Currently, research mainly focuses on adjusting the composite structure of $BiPO_4$ to improve its solar energy conversion efficiency and quantum yield [21]. Lu et al. used ion exchange to form in-situ Bi_2S_3 nanoparticles on the surface of $BiPO_4$ rods, achieving an 80% degradation rate of methylene blue under visible light irradiation within 3 h [22]. Zhang et al. prepared Ag/$BiPO_4$ composite photocatalysts using a combination of hydrothermal synthesis and impregnation methods, which showed much higher efficiency for the degradation of methylene blue under UV light irradiation compared to $BiPO_4$ alone [23]. Phosphates also provide clear directions and strategies for designing new photocatalysts. Oxygen vacancy defects are one of the important factors in improving photocatalytic efficiency [24–26]. In BiOBr, oxygen defect sites can capture photoexcited electrons, thereby reducing the recombination of electron-hole pairs and achieving spatial separation of photo-generated charge carriers. Introducing high-concentration oxygen vacancy defects can extend the range of the light response wavelength and increase photocatalytic activity. Research by Ren et al. showed that BiOX with oxygen vacancy defects can photocatalytically reduce CO_2 under simulated solar light irradiation, and oxygen vacancy defects can promote the adsorption and activation of CO_2 [27]. Chen et al. introduced oxygen vacancy (Ov) defects on the exposed surface of BiOBr nanosheets, modifying the band structure of BiOBr, enhancing its adsorption capacity, and lengthening the N≡N bond of adsorbed N_2 molecules [28].

This study aimed to prepare $BiPO_4$/Ov-BiOBr Type I heterojunction composites using a two-step solvothermal method to achieve exceptional visible-light photocatalytic performance for TC degradation and H_2O_2 generation [29–31]. The preparation parameters were adjusted to obtain optimal morphology, structure, and optical properties. The resulting composites were comprehensively characterized using various techniques. The photocatalytic degradation performance of the composites under visible-light irradiation was evaluated and compared with pure-phase $BiPO_4$ and Ov-BiOBr materials, revealing the advantages of heterojunction structures. The photocatalytic H_2O_2 generation performance of the composites under visible-light irradiation was investigated, and efforts were made to optimize photocatalytic efficiency by adjusting the composition and structure of the materials. The mechanisms of photocatalytic degradation and H_2O_2 generation were studied, with a focus on the generation, separation, migration, and consumption of photogenerated electron-hole pairs. Finally, the stability and reusability of the composites in photocatalytic processes were assessed through continuous cycling experiments, verifying their practicality and potential applications.

2. Results and Discussion

2.1. Crystal Structure Analysis

Figure 1 presents the X-ray diffraction (XRD) patterns of $BiPO_4$, Ov-BiOBr, and $BiPO_4$/Ov-BiOBr. The diffraction peaks of pure Ov-BiOBr and $BiPO_4$ in the XRD patterns match well with the standard data of BiOBr and $BiPO_4$ (BiOBr: PDF#73-2061; $BiPO_4$: PDF#15-0767). For $BiPO_4$/Ov-BiOBr composite, the diffraction peaks appearing at 2θ values of 21.4°, 25.3°, 29.1°, 31.2°, 38.6°, 41.6°, and 46.3° correspond to the (101), (111), (120), (012), (022), (031), and (310) crystal planes of $BiPO_4$, respectively, indicating the presence of $BiPO_4$ in the composite material [32,33]. The diffraction peaks appearing at 2θ values of 25.3°, 27.1°, 32.3°, 38.6°, and 46.3° correspond to the (111), (200), (110), (022), and (310) crystal planes of BiOBr, respectively, indicating the presence of BiOBr in the composite material [16,34]. Due to the effects of high temperature and ethylene glycol, the Bi-O bond on the $[Bi_2O_2]^{2+}$ layer breaks leading to the precipitation of some Bi atoms from the BiOBr lattice [34]. The diffraction peak at 2θ of 27.1° corresponds to the (012) crystal plane of Bi phase (PDF#85-1329). Furthermore, the significant decrease in the intensity of the (120) diffraction peak of $BiPO_4$ in the $BiPO_4$/Ov-BiOBr composite is likely due to the formation of a heterojunction structure between the (110) plane of $BiPO_4$ and BiOBr, thereby reducing its diffraction peak intensity. In Figure 1, it can be observed that the diffraction peaks of the

composite materials are significantly shifted to the right, indicating the strong interaction between the two components in the composite.

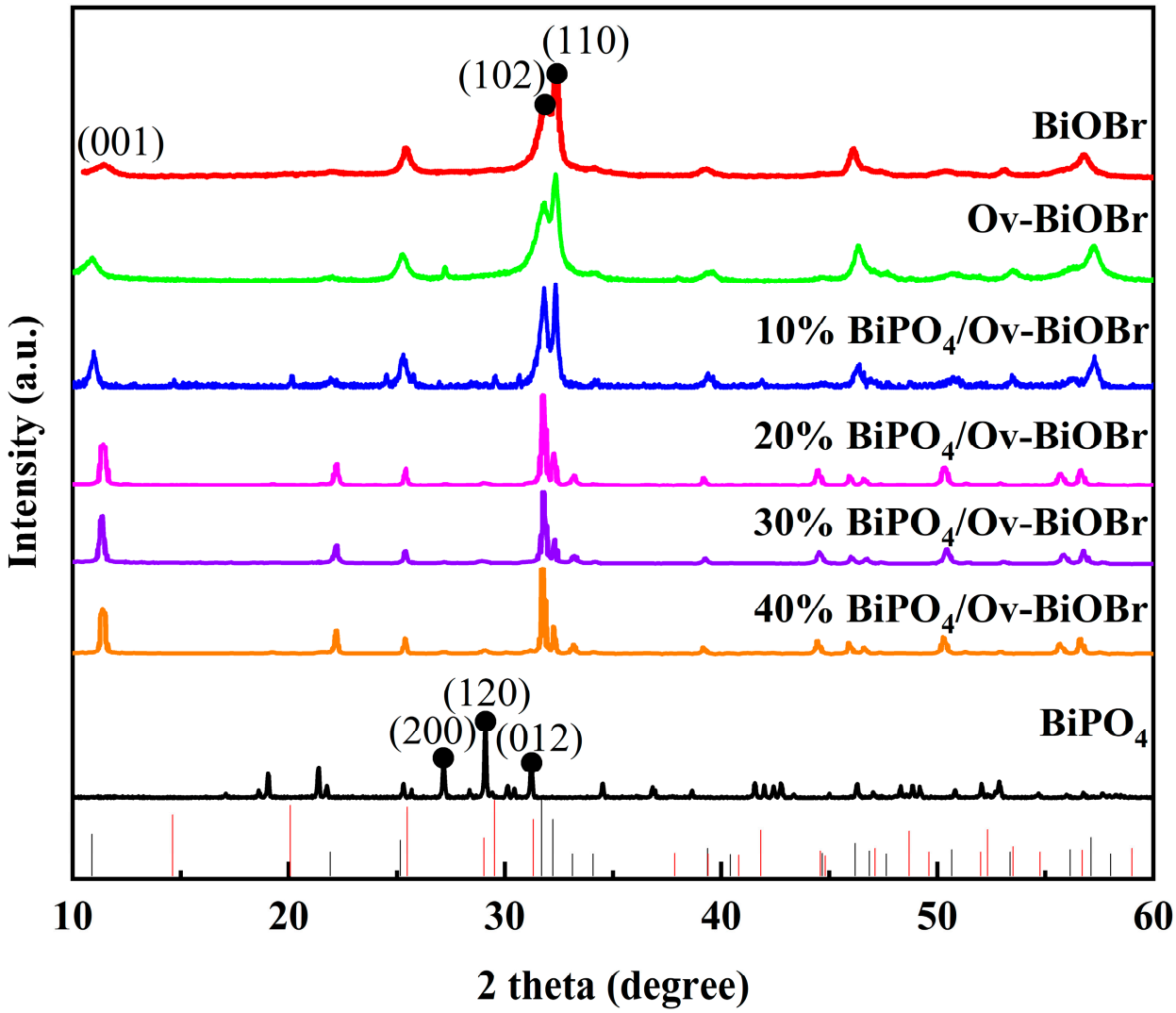

Figure 1. XRD patterns of Ov-BiOBr, $BiPO_4$ and $BiPO_4$/Ov-BiOBr composites.

2.2. TEM Analysis

Figure 2a shows the TEM image of the high-low heterojunction of $BiPO_4$/Ov-BiOBr, which reveals the nano-rod structure of $BiPO_4$ which is deposited on the spherical Ov-BiOBr. To confirm the nanorods as $BiPO_4$, the HRTEM images were analyzed, as shown in Figure 2b, which displays clear lattice fringes of $BiPO_4$ and good contact at the interface between $BiPO_4$ and Ov-BiOBr. The interplanar spacing of the (110) crystal plane in Ov-BiOBr was found to be 0.227 nm, while that of the (200) crystal plane in $BiPO_4$ was 0.327 nm [14,17]. At the interface of $BiPO_4$ and Ov-BiOBr, the main crystal plane of Bi was found to be (110), corresponding to interplanar spacing of 0.227 nm [13,34]. It is likely that the heterojunction was formed due to the in-situ deposition of $BiPO_4$ on the Bi sites in Ov-BiOBr [35–38]. The elemental mapping of Bi, Br, O, and P, as shown in Figure 2c–f, demonstrated that the O, Bi, Br, and P elements were evenly distributed on the $BiPO_4$/Ov-BiOBr composite photocatalyst [39]. These results indicate that the two-step hydrothermal method can effectively promote the in-situ deposition of $BiPO_4$ on Ov-BiOBr nanospheres, eventually forming the $BiPO_4$/Ov-BiOBr heterojunction.

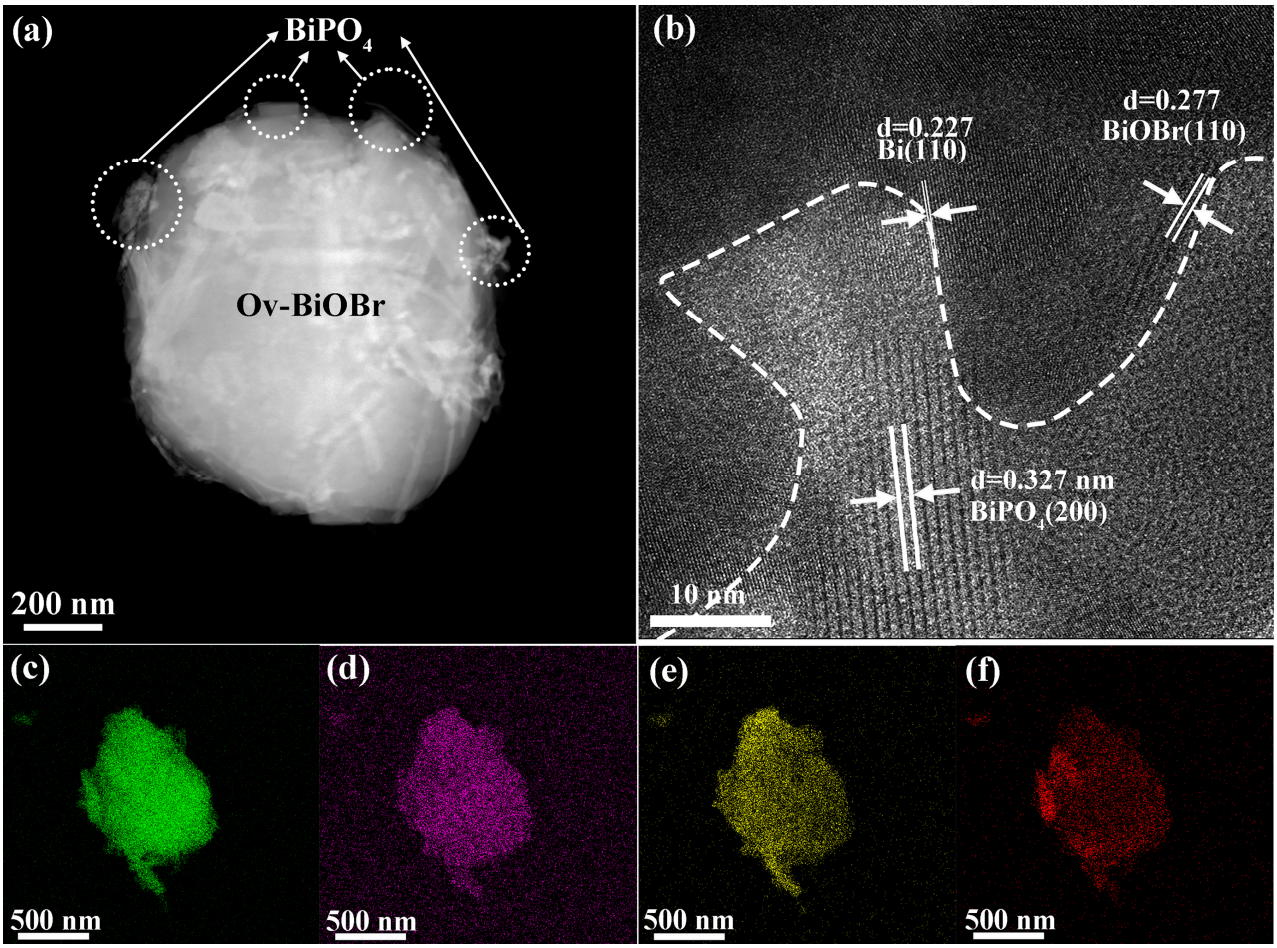

Figure 2. TEM image (**a**), HRTEM image (**b**), and elemental mapping of Bi (**c**), Br (**d**), O (**e**), and P (**f**) of $BiPO_4$/Ov-BiOBr.

2.3. XPS Analysis

The change in binding energy of elements can directly reflect the transfer of electrons and charge transfer processes in heterogeneous catalysts [40,41]. Therefore, monitoring the changes in binding energy can be used to study the direction of electron transfer in heterojunction photocatalysts [42]. In this study, in situ irradiation XPS analysis was performed on the $BiPO_4$/Ov-BiOBr composite before and after irradiation with a 300 W xenon lamp (420 nm < λ < 780 nm), and changes in the binding energies of Bi 4f, Br 3d, O 1s, and P 2p were observed. In the Bi 4f spectrum, the binding energy of Bi $4f_{5/2}$ decreased by 0.12 eV after irradiation, possibly due to electron transfer from PO_4^{3-} in $BiPO_4$ to BiOBr (Figure 3a) [17,43]. In the Br 3d spectrum, the binding energy of Br $3d_{5/2}$ decreased by 0.1 eV after irradiation, indicating a decrease in the electron density of BiOBr. These results indicate an increase in the electron density on BiOBr in the irradiated composite (Figure 3b). In the O 1s spectrum, the characteristic peak binding energies of lattice oxygen and surface hydroxyls at 533 eV and 529.9 eV increased by 0.1 eV after irradiation, possibly due to a decrease in the binding energy of OVs in the composite [44,45]. These changes indicate that the O in PO_4^{3-} provides electrons and transfers to BiOBr, and the O in the surface hydroxyls of $BiPO_4$ also provides electrons and participates in electron transfer (Figure 3c). In the P 2p spectrum, the binding energy of P 2p increased by 0.1 eV after irradiation, indicating an increase in the electron density of $BiPO_4$. This further confirms that electrons transfer from PO_4^{3-} in $BiPO_4$ to BiOBr (Figure 3d) [46]. Taken together, these results demonstrate the existence of the $BiPO_4$/Ov-BiOBr heterojunction and electron transfer between the heterojunctions.

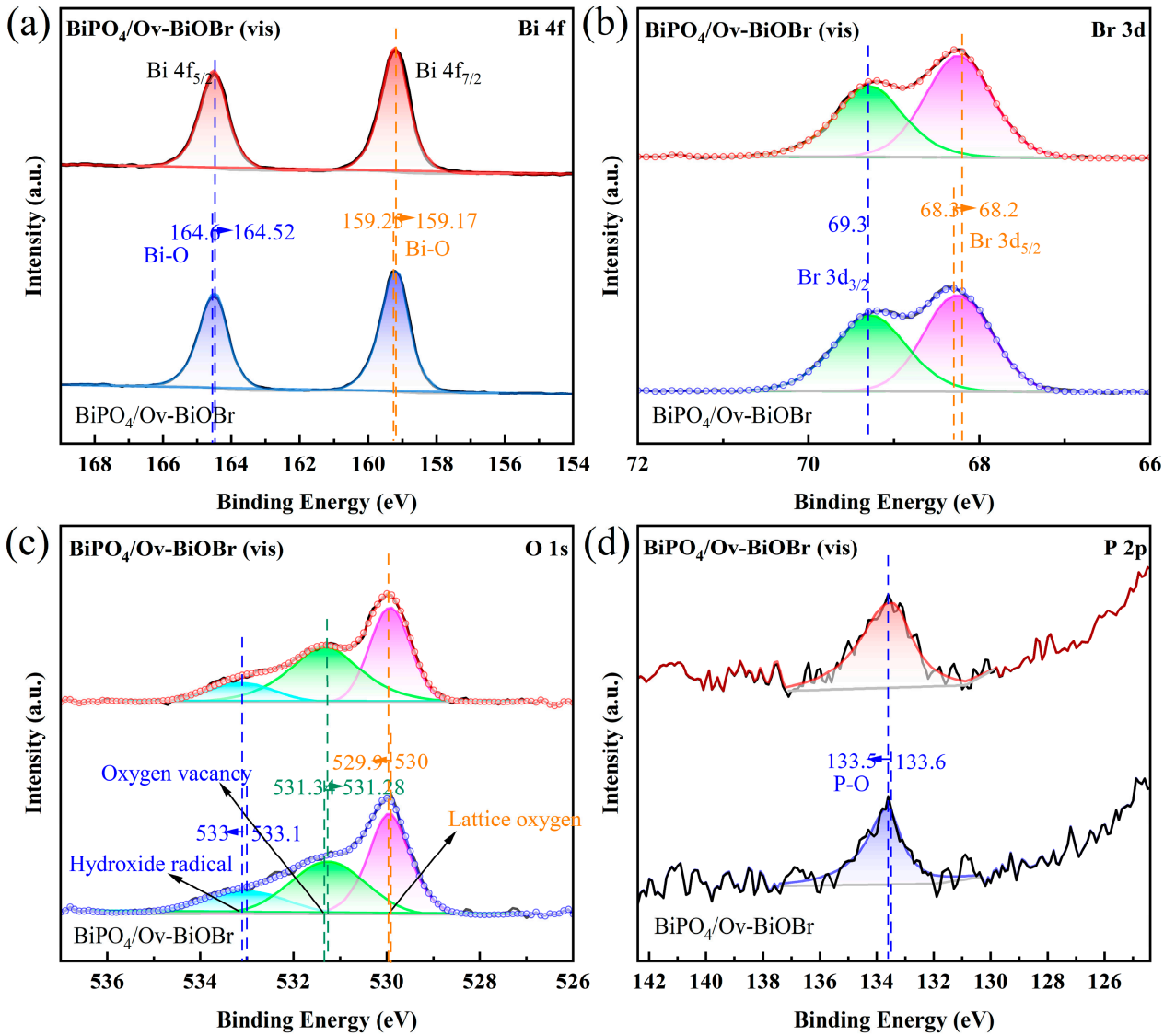

Figure 3. In situ irradiation XPS spectra of $BiPO_4$/Ov-BiOBr (**a**); high-resolution XPS maps of Bi 4f (**b**), Br 3d (**c**), O 1s (**d**) and P 2p (**e**).

Based on the experimental results, under visible light irradiation, the photogenerated electrons in the $BiPO_4$/Ov-BiOBr sample show a transfer direction from $BiPO_4$ to Ov-BiOBr. This finding provides strong evidence for the transfer direction of photogenerated electrons in $BiPO_4$/Ov-BiOBr heterojunction.

2.4. Raman Analysis

To verify the presence of precipitated metallic elemental Bi in Ov-BiOBr, Raman spectra of Ov-BiOBr and $BiPO_4$/Ov-BiOBr samples were analyzed (Figure 4). In the Raman spectrum of BiOBr, three distinct bands can be observed at 56 cm^{-1}, 112 cm^{-1}, and 374 cm^{-1}, respectively. The 56 cm^{-1} and 112 cm^{-1} Raman peaks correspond to the A1g external and Eg internal Bi-O stretching modes of BiOBr, while the relatively weaker peak at 374 cm^{-1} can be attributed to Eg and B1g bands caused by oxygen atom vibration [47]. For the $BiPO_4$/Ov-BiOBr composite, the band at 56 cm^{-1} can be attributed to the first-order scattering A1g mode of elemental Bi, the 112 cm^{-1} band corresponds to the A1g internal Bi-O stretching mode, and the 397 cm^{-1} band corresponds to Bi-O stretching [48,49]. These results further confirm the presence of precipitated metallic elemental Bi in Ov-BiOBr and

the distinct Raman spectral features of the $BiPO_4$/Ov-BiOBr composite as compared to those of BiOBr.

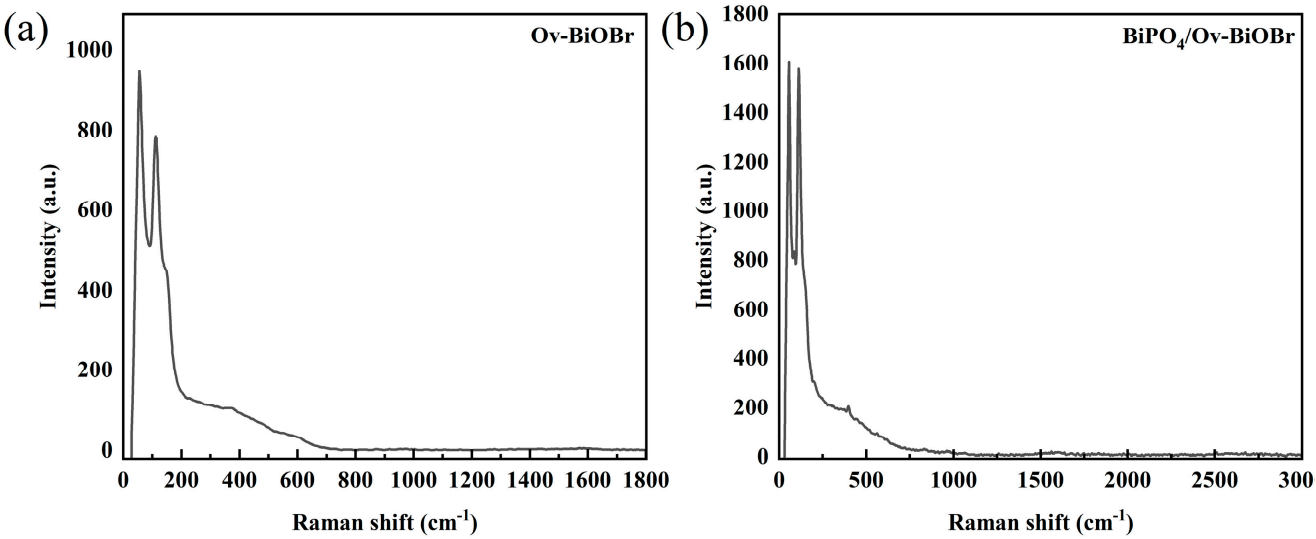

Figure 4. Raman spectra of Ov-BiOBr (**a**) and $BiPO_4$/Ov-BiOBr (**b**).

2.5. UV–Vis Diffuse Reflectance Spectra

To investigate the photoresponsive properties of $BiPO_4$/Ov-BiOBr photocatalyst, the band structure analysis is essential. The band structure of a photocatalyst is closely related to its photoresponsive properties. UV-Vis diffuse reflectance spectroscopy was used to analyze $BiPO_4$, Ov-BiOBr, and $BiPO_4$/Ov-BiOBr composite materials [50]. As shown in Figure 5a, the light absorption edge of $BiPO_4$ is between 300–400 nm, indicating that it is mainly responsive to UV light [51,52]. The light absorption edge of Ov-BiOBr is between 400–800 nm, indicating it has good visible light responsiveness. $BiPO_4$/Ov-BiOBr composite material has an absorption edge larger than 500 nm and strong visible light absorption characteristics. By converting the diffuse reflectance spectrum data, the band gap width diagrams of $BiPO_4$ and Ov-BiOBr can be obtained, as shown in Figure 5b. Extending the linear part of the curve to the intersection with the abscissa axis gives a band gap width of 4.2 eV and 2.7 eV for $BiPO_4$ and Ov-BiOBr, respectively. According to the formula Eg = E(VB) − E(CB), the valence band of $BiPO_4$ is 3.6 eV and the valence band of Ov-BiOBr is 2.22 eV. From the perspective of the band structure, n-type semiconductors with staggered band structures such as $BiPO_4$ and Ov-BiOBr can form effective heterojunctions.

2.6. Photoelectrochemical Properties

Band structure and light responsiveness are critical factors influencing the performance of photocatalysts. Therefore, in the photoelectrochemical experiments, we also detected and analyzed the Mott–Schottky (MS) curves of $BiPO_4$ and Ov-BiOBr [53]. Figure 6a,b show the MS curves at different frequencies, and the Erof values were calculated to be approximately −0.60 V and −0.38 V (vs. NHE, pH = 7) for $BiPO_4$ and Ov-BiOBr, respectively. In addition, we observed that the MS curves of $BiPO_4$ and Ov-BiOBr had a positive slope in the linear part, indicating that both materials have n-type semiconductor properties. According to the rule that the conduction band bottom potential of n-type semiconductors is approximately equal to the flat band potential, the conduction band potential (CB) of $BiPO_4$ was calculated to be −0.60 eV and that of Ov-BiOBr was −0.38 eV.

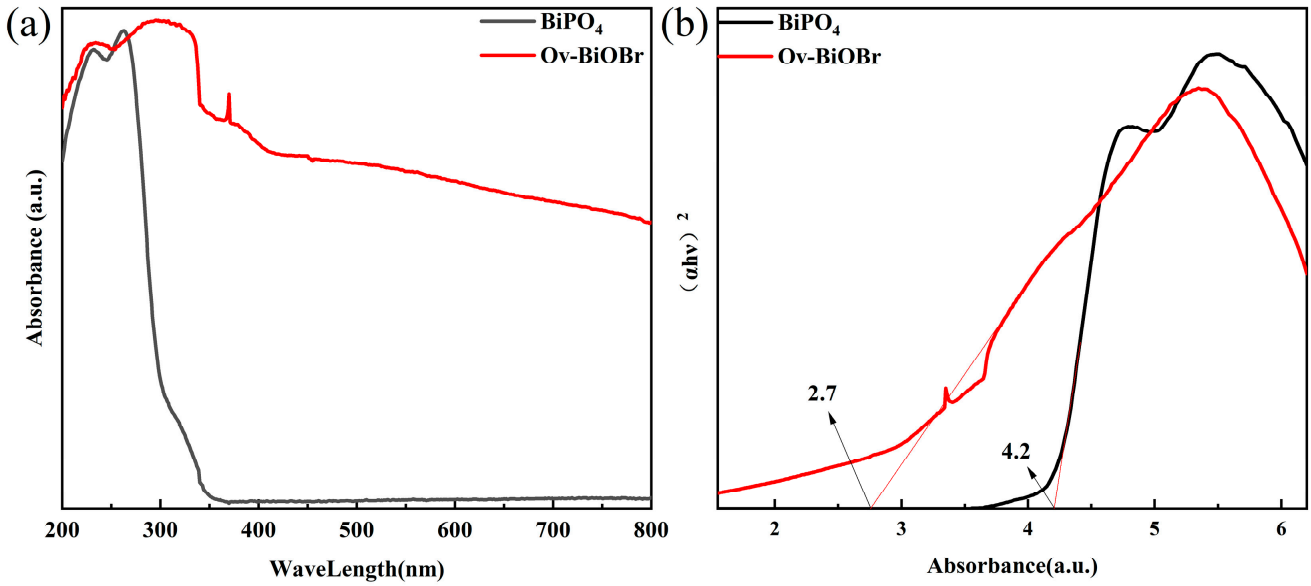

Figure 5. UV-Vis DRS (**a**) and forbidden band width (**b**) plots of the prepared samples.

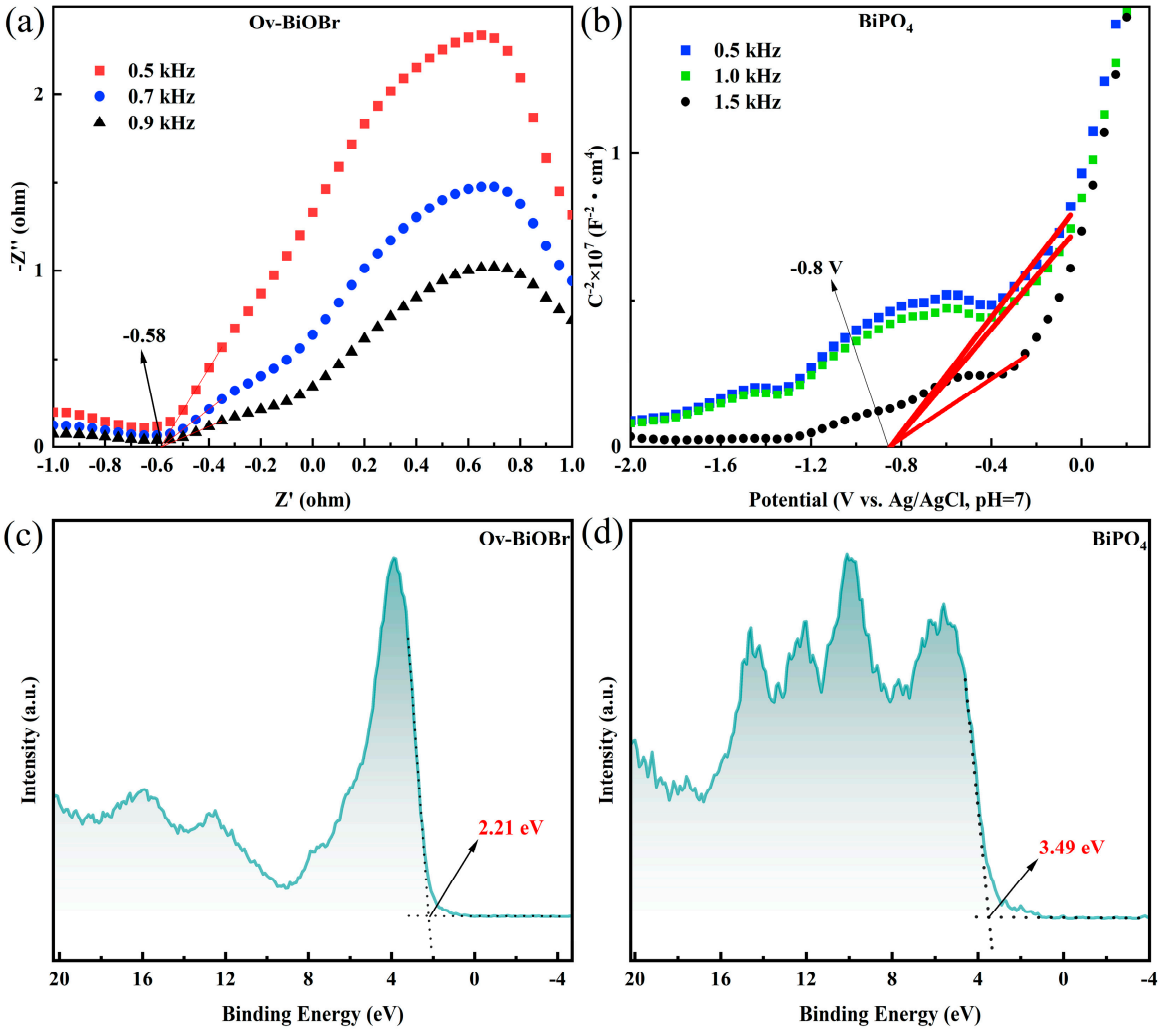

Figure 6. M-S plots (**a**,**b**) and VB-XPS (**c**,**d**) of Ov-BiOBr, $BiPO_4$.

Figure 6c,d show the VB-XPS spectra of Ov-BiOBr and $BiPO_4$. By reading the position of the intersection of the image, E_{vb} values of 2.21 and 3.49 eV for Ov-BiOBr and $BiPO_4$ were obtained, respectively. Considering the possibility of a potential difference between the sample and the instrument, we calculated the VB potential of Ov-BiOBr and $BiPO_4$ using the formula $E_{VB\text{-}NHE} = \varphi + E_{VB\text{-}XPS} - 4.44$, where φ is the instrument work function of the XPS analyzer (4.55 eV). Therefore, the EVB-NHE values of Ov-BiOBr and $BiPO_4$ are 2.32 and 3.6 eV, respectively. This is consistent with the results of the MS measurement of the valence band position. In conclusion, we have successfully determined the band structure of the $BiPO_4$/Ov-BiOBr heterojunction and demonstrated the successful formation of the $BiPO_4$/Ov-BiOBr composite with a type-I band alignment.

The photoelectrochemical measurements on $BiPO_4$, Ov-BiOBr, and 10% $BiPO_4$/Ov-BiOBr composite photocatalysts were performed. The photocurrent (Figure 7a) of pure $BiPO_4$ and pure Ov-BiOBr under visible light irradiation is 2 μA and 12 μA, respectively. Among all the composite catalysts, 10% $BiPO_4$/Ov-BiOBr displays the best photocurrent response (39 μA), which is three times that of Ov-BiOBr. In addition, the electrochemical impedance spectroscopy (EIS) diagram (Figure 7b) shows that 10% $BiPO_4$/Ov-BiOBr has smaller charge transfer resistance and larger transient photocurrent response. This indicates that the excellent photoelectrochemical performance of the 10% $BiPO_4$/Ov-BiOBr heterojunction can be attributed to its strong interface interaction, resulting in smaller photo-generated electron transfer resistance.

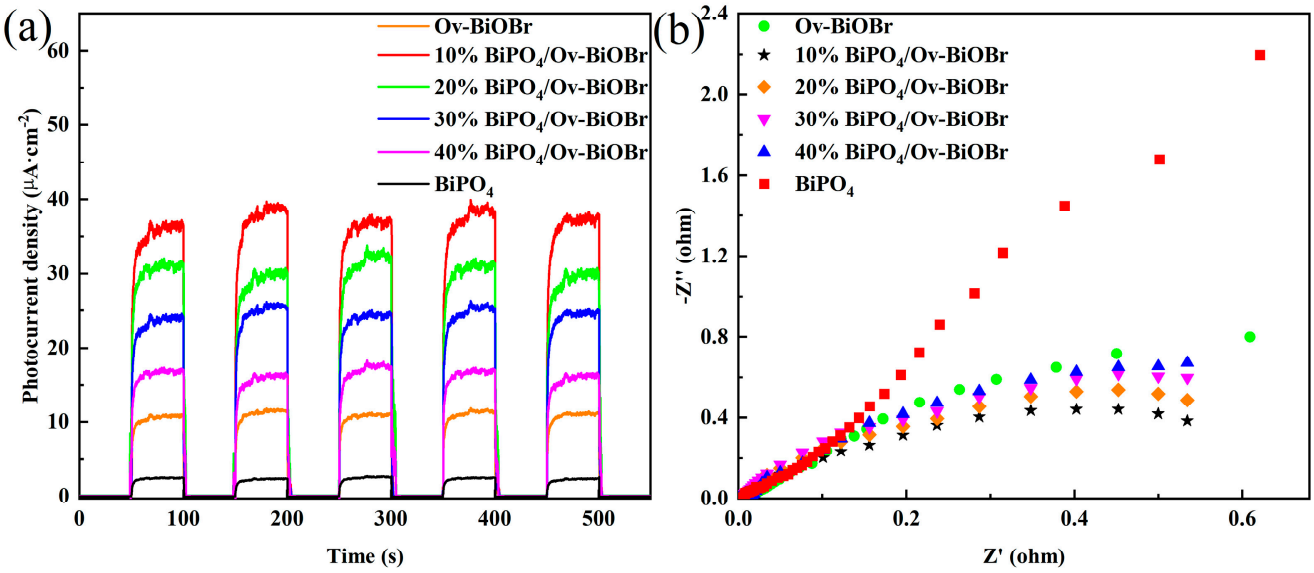

Figure 7. Photocurrent profiles (**a**) and impedance profiles (**b**) of the samples.

2.7. Photocatalytic Activity

The photocatalytic performance of samples was evaluated by the photocatalytic degradation experiment of tetracycline (TC). Compared to pure Ov-BiOBr, the composite material $BiPO_4$/Ov-BiOBr shows a significant enhancement in photocatalytic activity, with the 10% mol $BiPO_4$/Ov-BiOBr sample exhibiting the best degradation efficiency, degrading over 80% of TC under visible light irradiation in 30 min, far higher than other samples (Figure 8a). The photocatalytic degradation of TC by $BiPO_4$/Ov-BiOBr follows first-order reaction kinetics. As observed from Figure 8b, the reaction rate constants (K) of pure Ov-BiOBr, 10% $BiPO_4$/Ov-BiOBr, 20% $BiPO_4$/Ov-BiOBr, 30% $BiPO_4$/Ov-BiOBr, 40% $BiPO_4$/Ov-BiOBr, and pure $BiPO_4$ are 0.00944, 0.02534, 0.01376, 0.01043, 0.00991, and 0.00114 min^{-1}, respectively. The rate constant of 10% $BiPO_4$/Ov-BiOBr is 22, 2.68, 2.56, 2.42, and 1.84 times that of pure $BiPO_4$, pure Ov-BiOBr, 40% $BiPO_4$/Ov-BiOBr, 30% $BiPO_4$/Ov-BiOBr, and 20% $BiPO_4$/Ov-BiOBr, respectively. To detect the stability of $BiPO_4$/Ov-BiOBr, cyclic tests of TC photocatalytic degradation and XRD detection before and after illumination were carried

out (Figure 8c,d). The experimental results show that after four cycles of photocatalytic degradation, the degradation rate of TC by 10% $BiPO_4$/Ov-BiOBr still reached 90%. Subsequently, 39 more cycles were conducted, and after 3.25 days, the degradation efficiency decreased to 45%. The experiments indicate that the synthesized catalyst has relatively high stability. Meanwhile, the XRD pattern remained unchanged, indicating the relatively stable photocatalytic activity and structural stability of 10% $BiPO_4$/Ov-BiOBr during the photocatalytic process. The comparison of the degradation performance of the samples prepared in this study with other reported Bi-based photocatalysts is shown in Table 1.

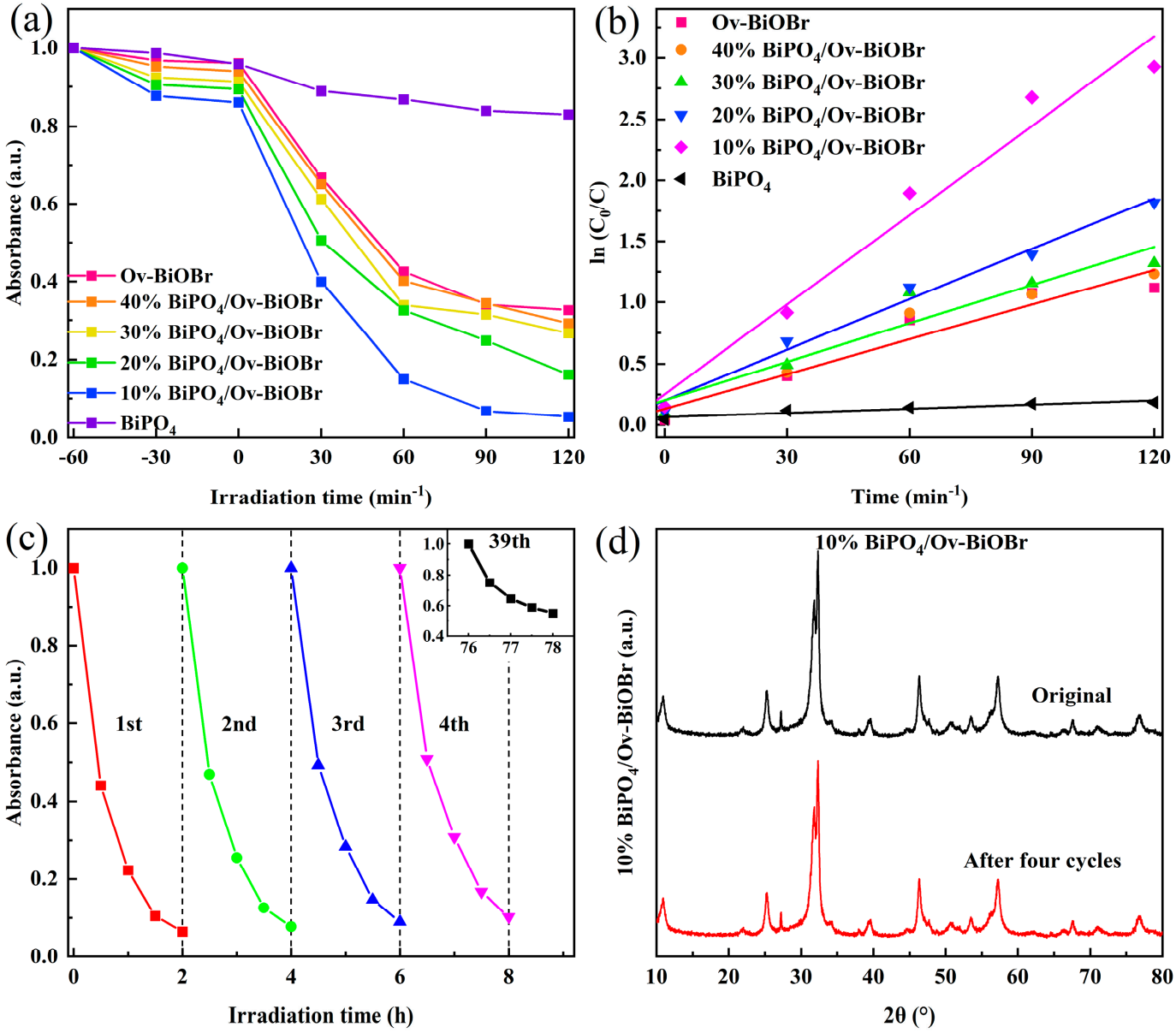

Figure 8. Photodegradation curve (**a**) and photodegradation kinetic curve (**b**) of TC; photodegradation cycle test curve (**c**) and XRD detection before and after illumination of $BiPO_4$/Ov-BiOBr (**d**).

Table 1. Recent work of BiOBr-based heterojunctions in degradation of TC.

Catalysts	Light Source (λ > 420 nm)	Concentration ($g \cdot L^{-1}$)	Pollutant ($mg \cdot L^{-1}$)	k (min^{-1})	References
$BiPO_4$/Ov-BiOBr	300 W Xe lamp	1	50(TC)	0.02534	This work
$W_{18}O_{49}$/BiOBr	300 W Xe lamp	1	20(TC)	0.014	[54]
UiO-66-NH_2/Bi/BiOBr	350 W Xe lamp	1	30(TC)	0.00838	[55]
CN@BOB-CQDs	LED light irradiation	1	20(TC)	0.221	[56]
BiOBr/Bi_2WO_6	500 W Xe lamp	1	10(TC)	0.0229	[57]
BiOBr/Bi_3O_4Br	500 W Xe lamp	1	10(TC)	0.02013	[58]

The study also investigated the photocatalytic activity of samples prepared under visible light irradiation (λ > 420 nm) for the in-situ production of H_2O_2 [59,60]. By substituting the absorbance peak values at different time points into the equation, the change in H_2O_2 concentration was calculated and a curve was plotted as shown in Figure 9. The results show that 10%$BiPO_4$/Ov-BiOBr has the best photocatalytic activity for producing H_2O_2, and after 120 min of visible light irradiation, the H_2O_2 concentration in the reactor reaches 139 $\mu mol \cdot L^{-1}$, which is 3.6 times that of BiOBr and 19 times that of $BiPO_4$. The free radical reaction process of this photocatalytic reaction includes $O_2 + 2e^- + 2H^+ \rightarrow H_2O_2$ (0.69 V vs. NHE) and $h^+ + OH^- \rightarrow \cdot OH + \cdot OH \rightarrow H_2O_2$ (2.29 V vs. NHE). Therefore, 10% $BiPO_4$/Ov-BiOBr obtained by solvothermal treatment may generate more photogenerated electrons and transfer them to the molecular surface for reacting with dissolved O_2. The successful construction of $BiPO_4$/Ov-BiOBr type I high-low junction retains the h^+ on the deep valence band of $BiPO_4$, thereby oxidizing OH^- to produce H_2O_2, which generates more H_2O_2 during the photocatalytic reaction. These results indicate that the nanoheterojunction photocatalyst with a more compact interface formed by solvothermal treatment is beneficial for improving the photocatalytic efficiency.

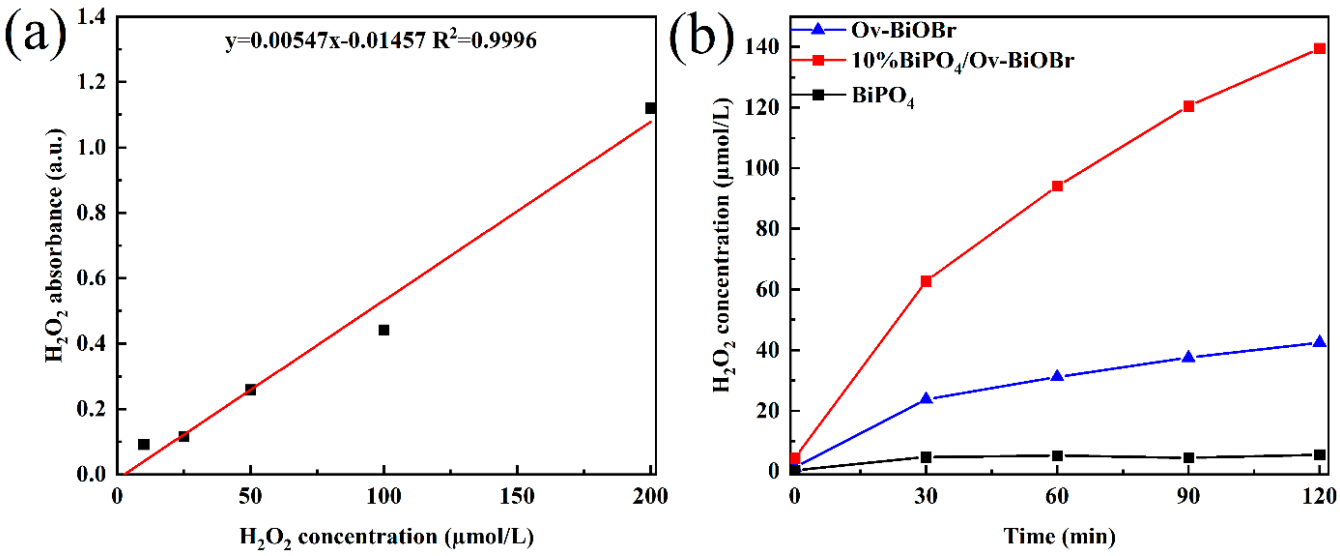

Figure 9. Concentration-absorbance curve of H_2O_2 (**a**); time-concentration curve of H_2O_2 produced under visible light irradiation (**b**).

2.8. Free Radical Capture

To further determine the main active species of $BiPO_4$/Ov-BiOBr in photocatalytic reactions, ESR and free radical capture experiments were conducted. The results are shown in Figure 10. IPA, BQ, and AO were used as free radical capture agents for ·OH, $\cdot O_2^-$, and h^+, respectively [18]. The experimental results show that ·OH and $\cdot O_2^-$ are the main active species in the TC photocatalytic degradation process. In addition, Figure 10b,c show the characteristic peaks of DMPO-·OH and DMPO-$\cdot O_2^-$ observed under visible light irradiation, while no signal was detected in the dark state. This indicates that ·OH and $\cdot O_2^-$

play a crucial role in the photocatalytic process of $BiPO_4$/Ov-BiOBr. The ESR free radical detection experiment further confirms the results of the free radical capture experiment, thereby determining that ·OH and $\cdot O_2^-$ are the main active species in the photocatalytic degradation reaction of $BiPO_4$/Ov-BiOBr.

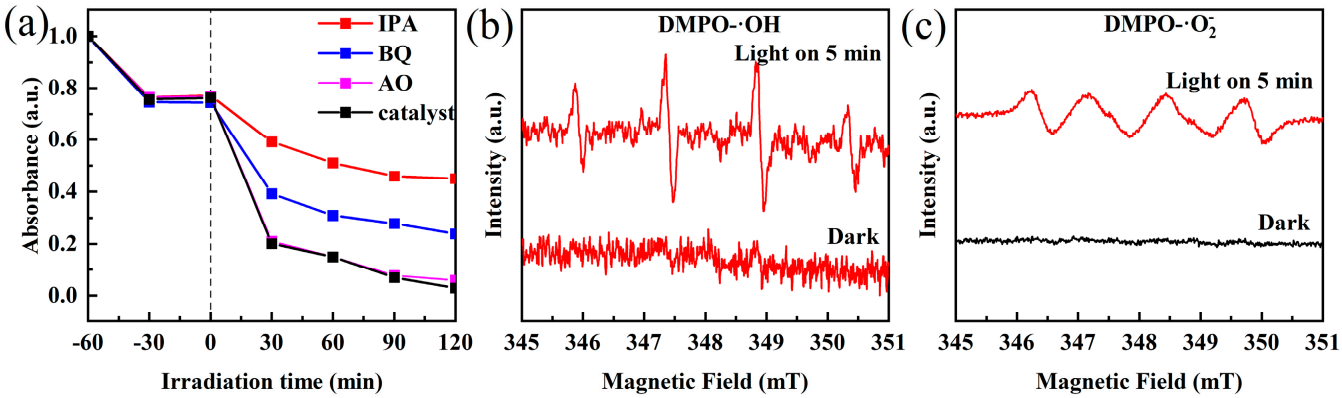

Figure 10. Experiments of radical trapping (**a**) ESR detection for 10% $BiPO_4$/Ov-BiOBr under dark and visible light irradiation: DMPO-·OH (**b**) and DMPO-$\cdot O_2^-$ (**c**).

2.9. Photocatalytic Mechanism

The difference in work function (Φ) or Fermi level (E_f) of semiconductor photocatalysts in heterojunction nanocomposites is considered an intrinsic driving force based on the VB-XPS measurement of the work function of Ov-BiOBr, $BiPO_4$, and $BiPO_4$/Ov-BiOBr; it can be observed that the material with a higher work function attracts electrons while the material with a lower work function loses electrons until the Fermi levels of both materials reach equilibrium. Consequently, an internal electric field (IEF) is formed at the interface, with the material with the higher work function being negatively charged and the material with the lower work function being positively charged [61,62]. Using the formula $\Phi = \Delta V + \varphi$ (where ΔV is the contact potential difference between the sample and the instrument sample holder, φ is the work function of the XPS analyzer, taken as 4.55 eV, and Φ is the work function of the sample) [30,63], the work functions of Ov-BiOBr, $BiPO_4$, and $BiPO_4$/Ov-BiOBr are calculated to be 6.18, 6.96, and 5.99 eV, respectively, and the distances between their two IP points are 1.63, 2.41, and 1.44 eV, respectively (Figure 11a–c). Since the Fermi level (E_{f1}) of $BiPO_4$ is lower than that of Ov-BiOBr (E_{f2}) (Figure 11d), when $BiPO_4$ comes into close contact with Ov-BiOBr, electrons will spontaneously diffuse from the material with the lower work function (Ov-BiOBr) to the material with the higher work function ($BiPO_4$) until the Fermi levels reach a new equilibrium (E_{f3}). After reaching equilibrium, an electron accumulation layer will form on the surface of $BiPO_4$, and an electron depletion layer will form on the surface of Ov-BiOBr, resulting in $BiPO_4$ being negatively charged and Ov-BiOBr being positively charged, thereby creating an IEF pointing from Ov-BiOBr to $BiPO_4$ (Figure 11e). This IEF provides a driving force for the directed movement of photogenerated charge carriers between different semiconductors. After photoexcitation, photogenerated electrons transfer from the conduction band of $BiPO_4$ to the conduction band of Ov-BiOBr, consistent with the results of in situ XPS measurement of electron transfer. Upon contact between the two semiconductors, the energy band of $BiPO_4$ and Ov-BiOBr will bend, leading to the migration of electrons from the conduction band of $BiPO_4$ to that of Ov-BiOBr. On the other hand, the photogenerated holes on the valence band of $BiPO_4$ will stay in place due to the band bending effect and Coulomb repulsion (Figure 11f). In summary, by matching the energy band structure, IEF, and energy band bending, the charge carriers with strong redox ability can be preserved, which creates conditions for improving photocatalytic activity.

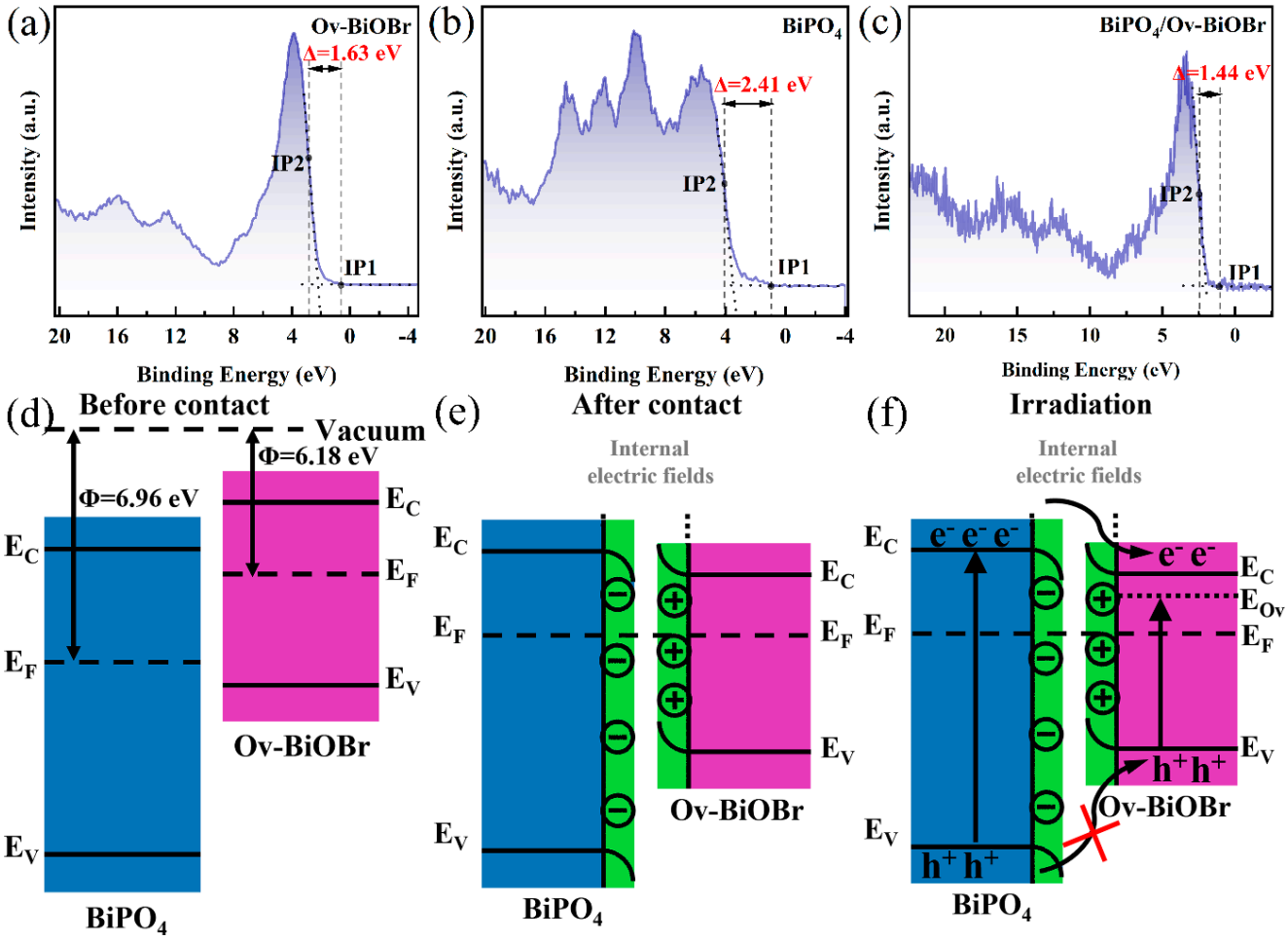

Figure 11. Work function of Ov-BiOBr, $BiPO_4$ and $BiPO_4$/Ov-BiOBr (**a**–**c**), carrier transfer mechanism of $BiPO_4$/Ov-BiOBr (**d**–**f**).

According to the experimental results, a possible reaction mechanism of the $BiPO_4$/Ov-BiOBr heterojunction photocatalyst is proposed (Figure 12). After illumination, the photogenerated electrons in $BiPO_4$ flow to Ov-BiOBr via the metallic Bi bridge, while the defect energy levels between the conduction and valence bands in Ov-BiOBr are excited [48,64–67]. Due to the effect of IEF and band bending, the holes in $BiPO_4$ cannot transfer to Ov-BiOBr. Therefore, the strongly oxidizing holes in $BiPO_4$ are retained. Since the conduction band potential of Ov-BiOBr is lower than that of dissolved oxygen, the photogenerated electrons on Ov-BiOBr can react with dissolved oxygen to produce $\cdot O_2^-$. In addition, the holes in $BiPO_4$ and Ov-BiOBr can effectively oxidize H_2O to generate ·OH. Since the ·OH has strong oxidizing properties, it can participate in the degradation of pollutants. Therefore, $\cdot O_2^-$ and ·OH are the main active species in the process of pollutant degradation. Based on the analysis of the energy band structure, electron transfer, work function, and active species detection results of the $BiPO_4$/Ov-BiOBr heterojunction, the possible charge transfer mechanism and reaction mechanism of the $BiPO_4$/Ov-BiOBr type I high-low junctions are proposed.

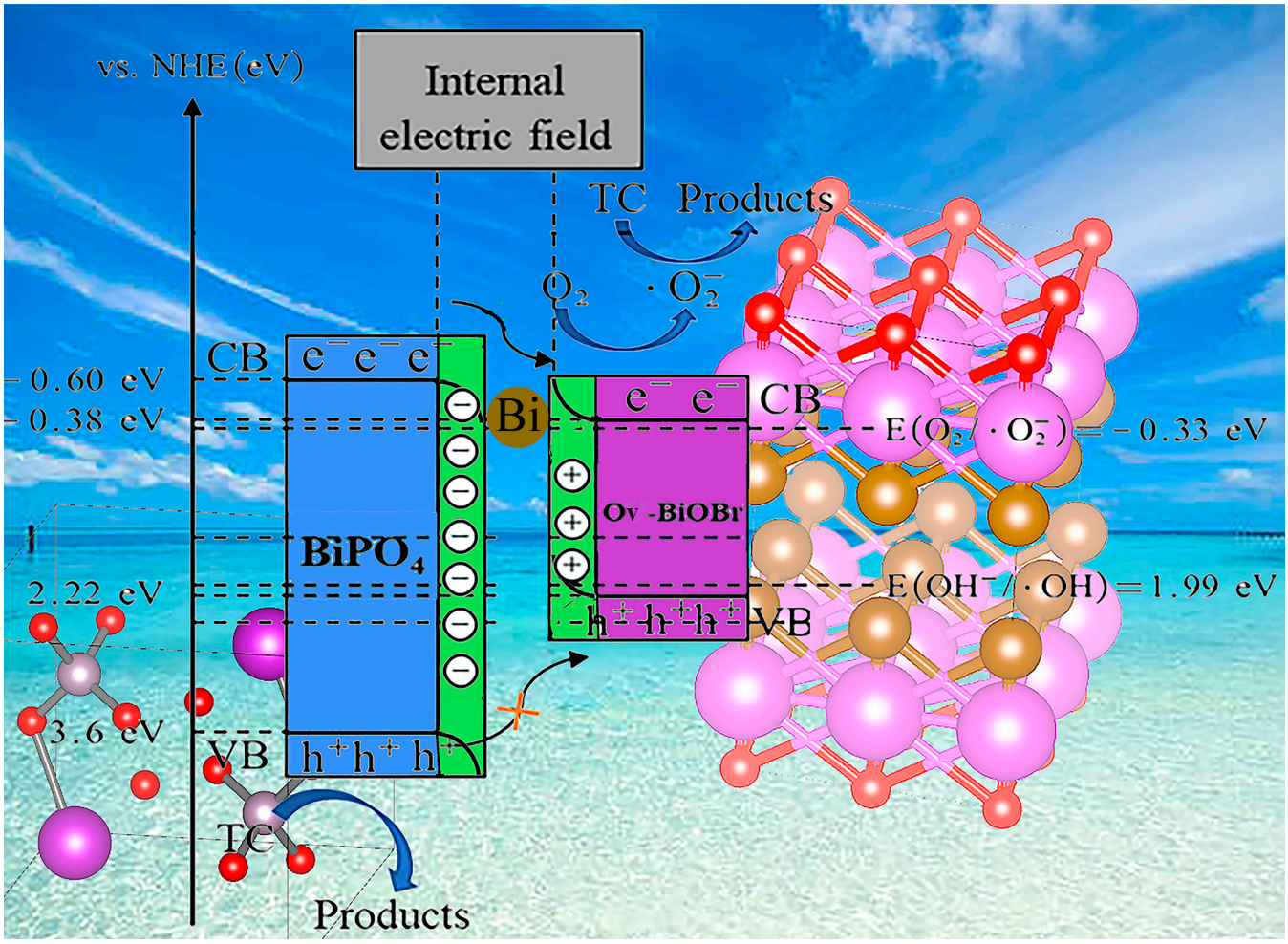

Figure 12. Photocatalytic mechanism of $BiPO_4$/Ov-BiOBr high-low junction.

3. Experimental Section

3.1. Chemicals

Bismuth nitrate pentahydrate ($Bi(NO_3)_3 \cdot 5H_2O$, 99%), potassium bromide (KBr, 99%), sodium dihydrogen phosphate (NaH_2PO_4, 99%), isopropanol (C_3H_8O), were purchased from Shanghai Tikem Industrial Co. Ethylene glycol ($(CH_2OH)_2$) (Shanghai, China) was purchased from Xilong Chemical Co. Tetracycline ($C_{22}H_{24}N_2O_8$) (Guangdong, China) was purchased from Shanghai Maclean Biochemical Technology Co. Anhydrous ethanol (CH_3CH_2OH) (Shanghai, China) was purchased from Xilong Science Co.

3.2. The Preparation of Ov-BiOBr

1 mmol $Bi(NO_3)_3 \cdot 5H_2O$ was added into 15 mL of ethylene glycol and stirred thoroughly to dissolve $Bi(NO_3)_3 \cdot 5H_2O$ completely in ethylene glycol, obtaining solution A [26]. Next, 1 mmol KBr was dissolved in 15 mL of ethylene glycol using the same method as for solution A, obtaining solution B. Solutions A and B were placed on a magnetic stirrer and stirred for 30 min at room temperature. Then, solution B was added dropwise into solution A and stirring was continued for 1 h. The mixed solution was transferred to a Teflon-lined autoclave and heated at 180 °C for 24 h. After cooling, the mixture was centrifuged at 9000 r/min for 5 min to ensure complete separation of the supernatant and the precipitate. The precipitate was repeatedly washed with ethanol and distilled water, and dried at 80 °C for 12 h. Finally, the sample was collected and ground as the precursor for the synthesis of the composite material [28,34,37].

3.3. The Preparation of $BiPO_4$ and $BiPO_4$/Ov-BiOBr

To prepare the $BiPO_4$/Ov-BiOBr heterojunction, a suitable amount of $Bi(NO_3)_3 \cdot 5H_2O$ was dispersed in 20 mL of distilled water. In another container, 50 mmol of Ov-BiOBr was dispersed in 20 mL of distilled water and sonicated for 30 min before being mixed with the $Bi(NO_3)_3 \cdot 5H_2O$ solution. Then, under vigorous stirring, an equimolar amount of NaH_2PO_4 compared to $Bi(NO_3)_3 \cdot 5H_2O$ was added dropwise into the mixed solution. The resulting mixture was transferred to a Teflon-lined high-pressure reaction vessel and heated at 170 °C for 12 h. After natural cooling, the sample was centrifuged to remove the supernatant and repeatedly washed with ethanol and distilled water. Finally, the sample was dried at 60 °C for 12 h. When preparing $BiPO_4$/Ov-BiOBr photocatalysts, different proportions of $BiPO_4$ (10%, 20%, 30%, and 40%) can be used to obtain various ratios. If Ov-BiOBr is not added, the resulting sample will be pure $BiPO_4$. The specific preparation process is shown in Figure 13.

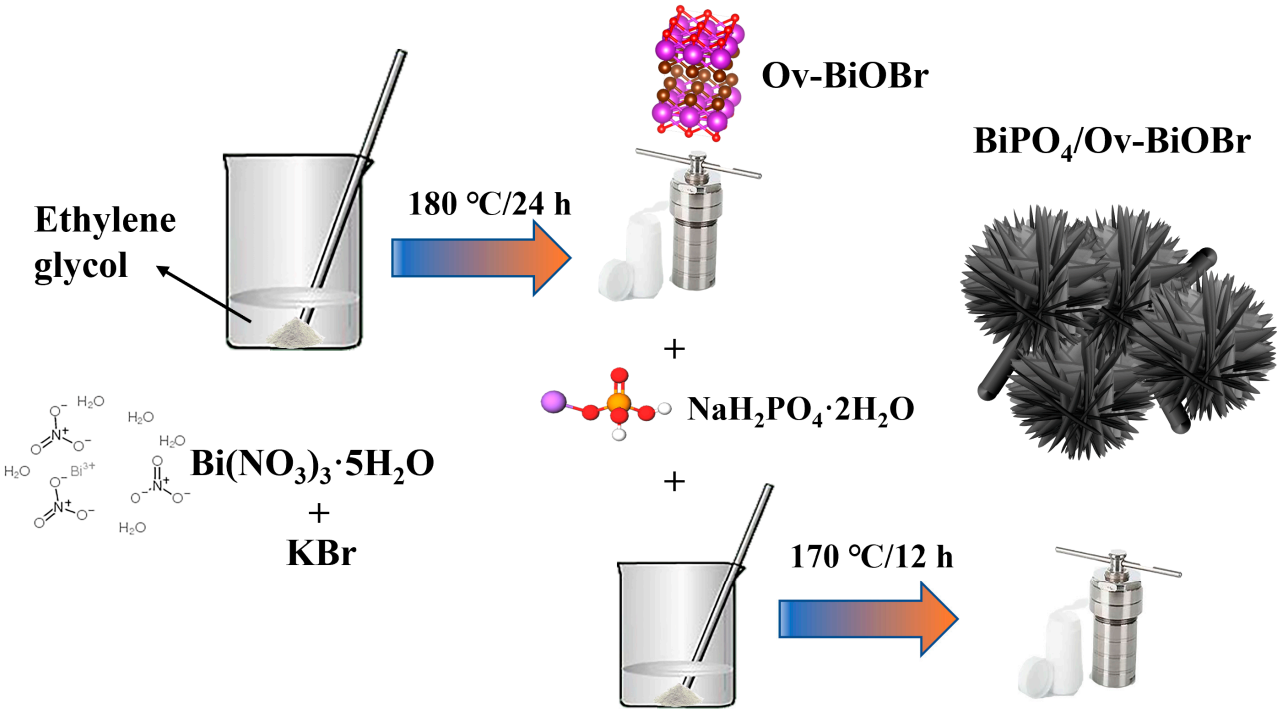

Figure 13. Preparation process of $BiPO_4$/Ov-BiOBr composite photocatalyst.

3.4. Chracterization

The crystal structures were analyzed using a D8 ADVANCE X-ray diffractometer (XRD, Bruker, Billerica, MA, USA). The morphology of $BiPO_4$/Ov-BiOBr was observed using a FEI Talos F200X transmission electron microscope (TEM, Waltham, MA, USA). Elemental analysis was performed using an Axis Ultra DLD X-ray photoelectron spectrometer (XPS, Kratos analytical, Manchester, UK). The Bi-O bond in Ov-BiOBr and $BiPO_4$/Ov-BiOBr was detected using Portman polarized Raman spectroscopy (e.g., Hengyuan, Shanghai, China). The UV-visible diffuse reflectance spectra (DRS) of Ov-BiOBr, $BiPO_4$, and $BiPO_4$/Ov-BiOBr were obtained using a UV-9000 H spectrophotometer (Metash, Shanghai, China) equipped with an integrating sphere. The photoelectrochemical properties of Ov-BiOBr, $BiPO_4$, and $BiPO_4$/Ov-BiOBr were analyzed using a CHI660E electrochemical analyzer (Chenhua, Shanghai, China) equipped with a three-electrode system. The degradation pathway of TC was analyzed using an LC-20A liquid chromatograph (Shimadzu, Kyoto, Japan). The detection of free radicals and characterization of defects in $BiPO_4$/Ov-BiOBr were tested using a JES-FA200 ESR spectrometer (JEOL, Tokyo, Japan).

3.5. Assessment of Photocatalytic Activity

In this experiment, the photocatalytic degradation performance of $BiPO_4$/Ov-BiOBr catalyst under visible light irradiation was investigated. Firstly, a 300 W xenon arc lamp (PLS-SXE 300, Beijing Perfectlight Technology Co., Ltd., Beijing, China) was fixed approximately 15 cm above a double-walled cylindrical quartz reactor. Then, 100 mg of photocatalyst powder with different ratios was mixed with 100 mL of tetracycline solution at a concentration of 50 mg·L^{-1}. With the light source turned off or blocked, the suspension underwent 30 min of dark adsorption and was stirred in the dark with a magnetic stirrer to establish a dynamic equilibrium between adsorption and desorption prior to illumination. To verify whether tetracycline would decompose under light, a control experiment was conducted. In this experiment, no catalyst was added, and the degradation of tetracycline (TC) was directly analyzed using a UV-visible spectrophotometer. During the experiment, approximately 4 mL of the suspension was withdrawn with a pipette every 30 min and transferred to a test tube. The suspension was centrifuged twice at 9000 r/min for 5 min each time to ensure complete separation of the supernatant and precipitate. Then, the supernatant was transferred with a plastic dropper to a colorimetric dish for absorbance and concentration measurements of degradation products. The qualitative detection of the target compound concentration was performed by detecting the specific absorption spectrum generated by the sample molecule upon excitation by UV or visible light. Quantitative analysis was carried out by determining the specific concentration of the target compound through the posiive correlation between the concentration and absorbance intensity of the same substance at the maximum absorption peak, as described by the Lambert–Beer law.

3.6. Active Species Trapping Experiments

Under the conditions of isopropyl alcohol (IPA, 10 mmol/L) and ammonium oxalate (AO, 10 mmol/L), the $BiPO_4$/Ov-BiOBr heterojunction was used for photocatalytic degradation of TC, while detecting the generation of hydroxyl radicals (·OH) and holes (h^+). To determine the presence of superoxide radicals (·O_2^-), an appropriate amount of photocatalyst was added to benzenequinone (BQ, 0.1 mmol/L), and the same experimental procedure for evaluating photocatalytic activity was performed. Finally, according to the Lambert–Beer law, the concentration of TC solution was analyzed at 423 nm using an UV-visible spectrophotometer equipped with an integrating sphere. ESR testing was conducted to further verify free radicals.

4. Conclusions

In summary, this study successfully synthesized a $BiPO_4$/Ov-BiOBr type-I high-low junction photocatalyst using a two-step solvothermal method, which exhibited higher photocatalytic activity compared to single $BiPO_4$ and Ov-BiOBr. The experimental results demonstrated that the $BiPO_4$ content had a significant impact on the catalyst performance, with the optimal addition amount being 10 mol%. The prepared sample displayed the best catalytic activity, with a reaction rate constant of 0.02534 min^{-1}, which was 2.3 times that of pure Ov-BiOBr. This was attributed to the synergistic effect of the bandgap matching between $BiPO_4$ and Ov-BiOBr, including factors such as charge transfer channels and efficient charge separation. Through free radical scavenging experiments, it was found that ·OH and ·O_2^- free radicals were the main active species in the photocatalytic process. This study provides a new approach for the development of efficient visible-light type-I high-low junction photocatalysts.

Author Contributions: Conceptualization, X.L. and Y.Z.; methodology, J.H.; software, Z.F.; validation, X.L., Y.Z. and J.H.; formal analysis, F.D.; investigation, Z.C.; resources, Z.F.; data curation, Z.C.; writing—original draft preparation, M.T.; writing—review and editing, X.L.; visualization, L.H.; supervision, F.D.; project administration, Y.X.; funding acquisition, X.L. All authors have read and agreed to the published version of the manuscript.

Funding: The research was funded by the National Natural Science Foundation of China (Grant No. 22262024, 51962023, 51862024, 51978324).

Data Availability Statement: The data generated during and/or analysed during the study are available from the corresponding author on reasonable request.

Acknowledgments: The authors acknowledge the financial support from the National Natural Science Foundation of China (Grant No. 22262024, 51962023, 51862024, 51978324), Zhejiang Province Key Research and Development Project (2023 C01191), the Double Thousand Talent Plan of Jiangxi Province, the Jiangxi Academic and Technical Leader of Major Disciplines (20213BCJL22053), the Key Laboratory of Jiangxi Province for Persistent Pollutants Control and Resources Recycling (Nanchang Hangkong University) (Grant No. ES202002077), Postgraduate Innovation Special Fund of NCHU (Nanchang Hangkong University), China (YC2021-003).

Conflicts of Interest: The authors declare no conflict of interest.

References

1. Chen, J.; Abazari, R.; Adegoke, K.A.; Maxakato, N.W.; Bello, O.S.; Tahir, M.; Tasleem, S.; Sanati, S.; Kirillov, A.M.; Zhou, Y. Metal–Organic Frameworks and Derived Materials as Photocatalysts for Water Splitting and Carbon Dioxide Reduction. *Coord. Chem. Rev.* **2022**, *469*, 214664. [CrossRef]
2. Sun, L.; Han, L.; Huang, J.; Luo, X.; Li, X. Single-Atom Catalysts for Photocatalytic Hydrogen Evolution: A Review. *Int. J. Hydrog. Energy* **2022**, *47*, 17583–17599. [CrossRef]
3. Zhao, C.; Zhang, Y.; Jiang, H.; Chen, J.; Liu, Y.; Liang, Q.; Zhou, M.; Li, Z.; Zhou, Y. Combined Effects of Octahedron NH_2 -UiO-66 and Flowerlike $ZnIn_2S_4$Microspheres for Photocatalytic Dye Degradation and Hydrogen Evolution under Visible Light. *J. Phys. Chem. C* **2019**, *123*, 18037–18049. [CrossRef]
4. Sun, L.-J.; Su, H.-W.; Xu, D.-F.; Wang, L.-L.; Tang, H.; Liu, Q.-Q. Carbon Hollow Spheres as Cocatalyst of Cu-Doped TiO_2 Nanoparticles for Improved Photocatalytic H_2 Generation. *Rare Met.* **2022**, *41*, 2063–2073. [CrossRef]
5. Lu, X.; Chen, F.; Qian, J.; Fu, M.; Jiang, Q.; Zhang, Q. Facile Fabrication of CeF_3/g-C_3N_4 Heterojunction Photocatalysts with Upconversion Properties for Enhanced Photocatalytic Desulfurization Performance. *J. Rare Earths* **2021**, *39*, 1204–1210. [CrossRef]
6. Li, X.; Liu, J.; Huang, J.; He, C.; Feng, Z.; Chen, Z.; Wan, L.; Deng, F. All Organic S-Scheme Heterojunction PDI-Ala/S-C_3N_4 Photocatalyst with Enhanced Photocatalytic Performance. *Acta Phys.-Chim. Sin.* **2021**, *37*, 2010030. [CrossRef]
7. Zhang, J.; Li, Z.; Meng, T.; Zang, S.; Yang, C.; Luo, X.; Wang, H.; Chen, J.; Jing, F.; Wang, C.; et al. Monolithic All-Weather Solar-Thermal Interfacial Membrane Evaporator. *Chem. Eng. J.* **2022**, *450*, 137893. [CrossRef]
8. Dong, S.; Zhao, Y.; Yang, J.; Liu, X.; Li, W.; Zhang, L.; Wu, Y.; Sun, J.; Feng, J.; Zhu, Y. Visible-Light Responsive PDI/RGO Composite Film for the Photothermal Catalytic Degradation of Antibiotic Wastewater and Interfacial Water Evaporation. *Appl. Catal. B Environ.* **2021**, *291*, 120127. [CrossRef]
9. Li, S.; Cai, M.; Liu, Y.; Wang, C.; Yan, R.; Chen, X. Constructing $Cd_{0.5}Zn_{0.5}S/Bi_2WO_6$ S-Scheme Heterojunction for Boosted Photocatalytic Antibiotic Oxidation and Cr(VI) Reduction. *Adv. Powder Mater.* **2023**, *2*, 100073. [CrossRef]
10. Guo, Y.; Yan, B.; Deng, F.; Shao, P.; Zou, J.; Luo, X.; Zhang, S.; Li, X. Lattice Expansion Boosting Photocatalytic Degradation Performance of $CuCo_2S_4$ with an Inherent Dipole Moment. *Chin. Chem. Lett.* **2023**, *34*, 107468. [CrossRef]
11. Li, S.; Cai, M.; Wang, C.; Liu, Y.; Li, N.; Zhang, P.; Li, X. Rationally designed Ta_3N_5/BiOCl S-scheme heterojunction with oxygen vacancies for elimination of tetracycline antibiotic and Cr(VI): Performance, toxicity evaluation and mechanism insight. *J. Mater. Sci. Technol.* **2022**, *123*, 177–190. [CrossRef]
12. Binas, V.D.; Sambani, K.; Maggos, T.; Katsanaki, A.; Kiriakidis, G. Synthesis and Photocatalytic Activity of Mn-Doped TiO_2 Nanostructured Powders under UV and Visible Light. *Appl. Catal. B-Environ.* **2012**, *113*, 79–86. [CrossRef]
13. Li, X.; Kang, B.; Dong, F.; Deng, F.; Han, L.; Gao, X.; Xu, J.; Hou, X.; Feng, Z.; Chen, Z.; et al. BiOBr with Oxygen Vacancies Capture 0D Black Phosphorus Quantum Dots for High Efficient Photocatalytic Ofloxacin Degradation. *Appl. Surf. Sci.* **2022**, *593*, 153422. [CrossRef]
14. Gao, M.; Zhang, D.; Pu, X.; Ma, H.; Su, C.; Gao, X.; Dou, J. Surface Decoration of BiOBr with $BiPO_4$ Nanoparticles to Build Heterostructure Photocatalysts with Enhanced Visible-Light Photocatalytic Activity. *Sep. Purif. Technol.* **2016**, *170*, 183–189. [CrossRef]
15. Wu, H.; Chen, R.; Wang, H.; Cui, W.; Li, J.; Wang, J.; Yuan, C.; Zhuo, L.; Zhang, Y.; Dong, F. An Atomic Insight into BiOBr/$La_2Ti_2O_7$ p-n Heterojunctions: Interfacial Charge Transfer Pathway and Photocatalysis Mechanism. *Catal. Sci. Technol.* **2020**, *10*, 826–834. [CrossRef]
16. Ye, X.; Li, Y.; Luo, P.; He, B.; Cao, X.; Lu, T. Iron Sites on Defective BiOBr Nanosheets: Tailoring the Molecular Oxygen Activation for Enhanced Photocatalytic Organic Synthesis. *Nano Res.* **2022**, *15*, 1509–1516. [CrossRef]
17. Liu, Z.S.; Wu, B.T.; Niu, J.N.; Feng, P.Z.; Zhu, Y.B. $BiPO_4$/BiOBr p–n Junction Photocatalysts: One-Pot Synthesis and Dramatic Visible Light Photocatalytic Activity. *Mater. Res. Bull.* **2015**, *63*, 187–193. [CrossRef]

18. Shi, J.; Meng, X.; Hao, M.; Cao, Z.; He, W.; Gao, Y.; Liu, J. Enhanced Photoactivity of $BiPO_4$/(001) Facet-Dominated Square BiOBr Flakes by Combining Heterojunctions with Facet Engineering Effects. *J. Phys. Chem. Solids* **2018**, *113*, 142–150. [CrossRef]
19. An, W.; Cui, W.; Liang, Y.; Hu, J.; Liu, L. Surface Decoration of $BiPO_4$ with BiOBr Nanoflakes to Build Heterostructure Photocatalysts with Enhanced Photocatalytic Activity. *Appl. Surf. Sci.* **2015**, *351*, 1131–1139. [CrossRef]
20. Pan, C.; Li, D.; Ma, X.; Chen, Y.; Zhu, Y. Effects of Distortion of PO_4 Tetrahedron on the Photocatalytic Performances of $BiPO_4$. *Catal. Sci. Technol.* **2011**, *1*, 1399–1405. [CrossRef]
21. Xu, H.; Xu, Y.; Li, H.; Xia, J.; Xiong, J.; Yin, S.; Huang, C.; Wan, H. Synthesis, Characterization and Photocatalytic Property of AgBr/$BiPO_4$ Heterojunction Photocatalyst. *Dalton Trans.* **2012**, *41*, 3387–3394. [CrossRef]
22. Lu, M.; Yuan, G.; Wang, Z.; Wang, Y.; Guo, J. Synthesis of $BiPO_4$/Bi_2S_3 Heterojunction with Enhanced Photocatalytic Activity under Visible-Light Irradiation. *Nanoscale Res. Lett.* **2015**, *10*, 385. [CrossRef]
23. Zhang, Y.; Fan, H.; Li, M.; Tian, H. Ag/$BiPO_4$ Heterostructures: Synthesis, Characterization and Their Enhanced Photocatalytic Properties. *Dalton Trans.* **2013**, *42*, 13172–13178. [CrossRef]
24. Zhu, C.; Zhu, M.; Sun, Y.; Zhou, Y.; Gao, J.; Huang, H.; Liu, Y.; Kang, Z. Carbon-Supported Oxygen Vacancy-Rich Co_3O_4 for Robust Photocatalytic H_2O_2 Production via Coupled Water Oxidation and Oxygen Reduction Reaction. *ACS Appl. Energy Mater.* **2019**, *2*, 8737–8746. [CrossRef]
25. Li, Y.; Liu, T.; Cheng, Z.; Peng, Y.; Yang, S.; Zhang, Y. Facile Synthesis of High Crystallinity and Oxygen Vacancies Rich Bismuth Oxybromide Upconversion Nanosheets by Air-Annealing for UV-Vis-NIR Broad Spectrum Driven Bisphenol A Degradation. *Chem. Eng. J.* **2021**, *421*, 127868. [CrossRef]
26. Sun, Z.; Yang, X.; Yu, X.-F.; Xia, L.; Peng, Y.; Li, Z.; Zhang, Y.; Cheng, J.; Zhang, K.; Yu, J. Surface Oxygen Vacancies of Pd/Bi_2MoO_{6-x} Acts as "Electron Bridge" to Promote Photocatalytic Selective Oxidation of Alcohol. *Appl. Catal. B Environ.* **2021**, *285*, 119790. [CrossRef]
27. Ren, X.; Gao, M.; Zhang, Y.; Zhang, Z.; Cao, X.; Wang, B.; Wang, X. Photocatalytic Reduction of CO_2 on BiOX: Effect of Halogen Element Type and Surface Oxygen Vacancy Mediated Mechanism. *Appl. Catal. B Environ.* **2020**, *274*, 119063. [CrossRef]
28. Chen, X.; Zhang, X.; Li, Y.-H.; Qi, M.-Y.; Li, J.-Y.; Tang, Z.-R.; Zhou, Z.; Xu, Y.-J. Transition Metal Doping BiOBr Nanosheets with Oxygen Vacancy and Exposed {102} Facets for Visible Light Nitrogen Fixation. *Appl. Catal. B Environ.* **2021**, *281*, 119516. [CrossRef]
29. Hu, Y.; Li, X.; Wang, W.; Deng, F.; Han, L.; Gao, X.; Feng, Z.; Chen, Z.; Huang, J.; Zeng, F.; et al. Bi and S Co-doping g-C_3N_4 to Enhance Internal Electric Field for Robust Photocatalytic Degradation and H_2 Production. *Chin. J. Struct. Chem.* **2022**, *41*, 2206069–2206078. [CrossRef]
30. Xiong, J.; Li, X.; Huang, J.; Gao, X.; Chen, Z.; Liu, J.; Li, H.; Kang, B.; Yao, W.; Zhu, Y. CN/RGO@BPQDs High-Low Junctions with Stretching Spatial Charge Separation Ability for Photocatalytic Degradation and H_2O_2 Production. *Appl. Catal. B Environ.* **2020**, *266*, 118602. [CrossRef]
31. Yan, B.; Peng, J.; Deng, F.; Liu, L.; Li, X.; Shao, P.; Zou, J.; Zhang, S.; Wang, J.; Luo, X. Novel $ZnFe_2O_4$/Bi_2S_3 High-Low Junctions for Boosting Tetracycline Degradation and Cr(VI) Reduction. *Chem. Eng. J.* **2023**, *452*, 139353. [CrossRef]
32. Zhang, Z.; Liu, H.; Xu, J.; Zeng, H. CuTCPP/$BiPO_4$ Composite with Enhanced Visible Light Absorption and Charge Separation. *J. Photochem. Photobiol. A Chem.* **2017**, *336*, 25–31. [CrossRef]
33. Pan, C.; Xu, J.; Wang, Y.; Li, D.; Zhu, Y. Dramatic Activity of C_3N_4/$BiPO_4$ Photocatalyst with Core/Shell Structure Formed by Self-Assembly. *Adv. Funct. Mater.* **2012**, *22*, 1518–1524. [CrossRef]
34. Li, X.; Liu, Q.; Deng, F.; Huang, J.; Han, L.; He, C.; Chen, Z.; Luo, Y.; Zhu, Y. Double-Defect-Induced Polarization Enhanced O_V-BiOBr/$Cu_{2-X}S$ High-Low Junction for Boosted Photoelectrochemical Hydrogen Evolution. *Appl. Catal. B-Environ.* **2022**, *314*, 121502. [CrossRef]
35. Zhu, K.; Yao, W.; Zhu, Y. Preparation of Bismuth Phosphate Photocatalyst with High Dispersion by Refluxing Method. *Acta Phys. -Chim. Sin.* **2016**, *32*, 1519–1526. [CrossRef]
36. Jin, M.; Lu, S.; Ma, L.; Gan, M. One-Step Synthesis of in Situ Reduced Metal Bi Decorated Bismuth Molybdate Hollow Microspheres with Enhancing Photocatalytic Activity. *Appl. Surf. Sci.* **2017**, *396*, 438–443. [CrossRef]
37. Ma, H.; Zhao, M.; Xing, H.; Fu, Y.; Zhang, X.; Dong, X. Synthesis and Enhanced Photoreactivity of Metallic Bi-Decorated BiOBr Composites with Abundant Oxygen Vacancies. *J. Mater. Sci.-Mater. Electron.* **2015**, *26*, 10002–10011. [CrossRef]
38. Liu, J.; Wang, T.; Nie, Q.; Hu, L.; Cui, Y.; Tan, Z.; Yu, H. One-Step Synthesis of Metallic Bi Deposited Bi_2WO_6 Nanoclusters for Enhanced Photocatalytic Performance: An Experimental and DFT Study. *Appl. Surf. Sci.* **2021**, *559*, 149970. [CrossRef]
39. Zhu, J.; Li, Y.; Wang, X.; Zhao, J.; Wu, Y.; Li, F. Simultaneous Phosphorylation and Bi Modification of BiOBr for Promoting Photocatalytic CO_2 Reduction. *ACS Sustain. Chem. Eng.* **2019**, *7*, 14953–14961. [CrossRef]
40. Tougaard, S. Practical Guide to the Use of Backgrounds in Quantitative XPS. *J. Vac. Sci. Technol. A* **2021**, *39*, 011201. [CrossRef]
41. Catalin, N.; Cernea, M. Characterization of $BaTi_4O_9$ Ceramics by Raman Spectroscopy and XPS after Ion Etching. *J. Optoelectron. Adv. Mater.* **2006**, *8*, 1879–1883.
42. Xia, P.; Cao, S.; Zhu, B.; Liu, M.; Shi, M.; Yu, J.; Zhang, Y. Designing a 0D/2D S-Scheme Heterojunction over Polymeric Carbon Nitride for Visible-Light Photocatalytic Inactivation of Bacteria. *Angew. Chem. Int. Ed.* **2020**, *59*, 5218–5225. [CrossRef]

43. Zou, X.; Dong, Y.; Zhang, X.; Cui, Y.; Ou, X.; Qi, X. The Highly Enhanced Visible Light Photocatalytic Degradation of Gaseous o-Dichlorobenzene through Fabricating like-Flowers $BiPO_4$/BiOBr p-n Heterojunction Composites. *Appl. Surf. Sci.* **2017**, *391*, 525–534. [CrossRef]
44. Xu, L.; Jiang, D.; Zhao, Y.; Yan, P.; Dong, J.; Qian, J.; Ao, H.; Li, J.; Yan, C.; Li, H. Integrated $BiPO_4$ Nanocrystal/BiOBr Heterojunction for Sensitive Photoelectrochemical Sensing of 4-Chlorophenol. *Dalton Trans.* **2018**, *47*, 13353. [CrossRef] [PubMed]
45. Zhang, H.; Zhao, L.; Wang, L.; Hao, J.; Meng, X. Fabrication of Oxygen-Vacancy-Rich Black-BiOBr/BiOBr Heterojunction with Enhanced Photocatalytic Activity. *J. Mater. Sci.* **2020**, *55*, 10785–10795. [CrossRef]
46. Hu, X.; Li, C.; Song, J.; Zheng, S.; Sun, Z. Multidimensional Assembly of Oxygen Vacancy-Rich Amorphous TiO_2-BiOBr-Sepiolite Composite for Rapid Elimination of Formaldehyde and Oxytetracycline under Visible Light. *J. Colloid Interface Sci.* **2020**, *574*, 61–73. [CrossRef]
47. Sultana, R.; Gurjar, G.; Gahtori, B.; Patnaik, S.; Awana, V.P.S. Flux Free Single Crystal Growth and Detailed Physical Property Characterization of $Bi_{1-X}Sb_X$ (X = 0.05, 0.1 and 0.15) Topological Insulator. *Mater. Res. Express* **2019**, *6*, 106102. [CrossRef]
48. Deng, F.; Zhang, Q.; Yang, L.; Luo, X.; Wang, A.; Luo, S.; Dionysiou, D.D. Visible-Light-Responsive Graphene-Functionalized Bi-Bridge Z-Scheme Black BiOCl/Bi_2O_3 Heterojunction with Oxygen Vacancy and Multiple Charge Transfer Channels for Efficient Photocatalytic Degradation of 2-Nitrophenol and Industrial Wastewater Treatment. *Appl. Catal. B Environ.* **2018**, *238*, 61–69. [CrossRef]
49. Zhu, B.; Hong, X.; Tang, L.; Liu, Q.; Tang, H. Enhanced Photocatalytic CO_2 Reduction over 2D/1D $BiOBr_{0.5}Cl_{0.5}/WO_3$ S-Scheme Heterostructure. *Acta Phys. -Chim. Sin.* **2022**, *38*, 2111008. [CrossRef]
50. Dong, S.; Cui, L.; Tian, Y.; Xia, L.; Wu, Y.; Yu, J.; Bagley, D.M.; Sun, J.; Fan, M. A Novel and High-Performance Double Z-Scheme Photocatalyst ZnO-SnO_2-Zn_2SnO_4 for Effective Removal of the Biological Toxicity of Antibiotics. *J. Hazard. Mater.* **2020**, *399*, 123017. [CrossRef]
51. Kumar, A.; Sharma, S.K.; Sharma, G.; Al-Muhtaseb, A.H.; Naushad, M.; Ghfar, A.A.; Stadler, F.J. Wide Spectral Degradation of Norfloxacin by Ag@$BiPO_4$/BiOBr/$BiFeO_3$ Nano-Assembly: Elucidating the Photocatalytic Mechanism under Different Light Sources. *J. Hazard. Mater.* **2019**, *364*, 429–440. [CrossRef] [PubMed]
52. Chu, L.; Han, X.; Zhang, J.; Jiang, S.; Xue, R.; Dong, S.; Sun, J. $BiPO_4$ Coupled Bi^{3+} Doping SnO_2 QDs with Improved Performance towards Various Organic Pollutants Clearance. *Colloids Surf. A Physicochem. Eng. Asp.* **2021**, *612*, 125915. [CrossRef]
53. Li, X.; Xiong, J.; Gao, X.; Ma, J.; Chen, Z.; Kang, B.; Liu, J.; Li, H.; Feng, Z.; Huang, J. Novel BP/BiOBr S-Scheme Nano-Heterojunction for Enhanced Visible-Light Photocatalytic Tetracycline Removal and Oxygen Evolution Activity. *J. Hazard. Mater.* **2020**, *387*, 121690. [CrossRef] [PubMed]
54. Ji, S.; Dong, J.; Ji, M.; Zou, W.; Yin, S.; Chen, Z.; Xia, J. Rapid Dual-Channel Electrons Transfer via Synergistic Effect of LSPR Effect and Build-in Electric Field in Z-Scheme $W_{18}O_{49}$/BiOBr Heterojunction for Organic Pollutants Degradation. *Inorg. Chem. Commun.* **2022**, *138*, 109283. [CrossRef]
55. Zhang, X.; Cao, W.; Chen, C.; Jiang, C.; Wang, Y. Photocatalytic Activity and Degradation Mechanism of In-Situ Reduction Bi-Doped Self-Assembled 3D Flower-Sphere UiO-66-NH_2/BiOBr. *Opt. Mater. X* **2021**, *12*, 100090. [CrossRef]
56. Huang, L.; Liu, J.; Li, P.; Li, Y.; Wang, C.; Shu, S.; Song, Y. CQDs Modulating Z-Scheme g-C_3N_4/BiOBr Heterostructure for Photocatalytic Removing RhB, BPA and TC and E. *Coli by LED Light. J. Alloys Compd.* **2022**, *895*, 162637. [CrossRef]
57. Liu, Y.; He, J.; Qi, Y.; Wang, Y.; Long, F.; Wang, M. Preparation of Flower-like BiOBr/Bi_2WO_6 Z-Scheme Heterojunction through an Ion Exchange Process with Enhanced Photocatalytic Activity. *Mater. Sci. Semicond. Process.* **2022**, *137*, 106195. [CrossRef]
58. Zhang, F.; Xiao, X.; Xiao, Y. In Situ Fabrication of Type II 3D Hierarchical Flower-like BiOBr/Bi_3O_4Br Heterojunction with Improved Photocatalytic Activity. *J. Alloys Compd.* **2022**, *923*, 166417. [CrossRef]
59. Wang, W.; Li, X.; Deng, F.; Liu, J.; Gao, X.; Huang, J.; Xu, J.; Feng, Z.; Chen, Z.; Han, L. Novel Organic/Inorganic PDI-Urea/BiOBr S-Scheme Heterojunction for Improved Photocatalytic Antibiotic Degradation and H_2O_2 Production. *Chin. Chem. Lett.* **2022**, *33*, 5200–5207. [CrossRef]
60. Zan, Z.; Li, X.; Gao, X.; Huang, J.; Luo, Y.; Han, L. 0D/2D Carbon Nitride Quantum Dots (CNQDs)/BiOBr S-Scheme Heterojunction for Robust Photocatalytic Degradation and H_2O_2 Production. *Acta Phys.-Chim. Sin.* **2023**, *39*, 2209016. [CrossRef]
61. Yuan, J.; Liu, X.; Tang, Y.; Zeng, Y.; Wang, L.; Zhang, S.; Cai, T.; Liu, Y.; Luo, S.; Pei, Y.; et al. Positioning Cyanamide Defects in G-C_3N_4: Engineering Energy Levels and Active Sites for Superior Photocatalytic Hydrogen Evolution. *Appl. Catal. B Environ.* **2018**, *237*, 24–31. [CrossRef]
62. Dong, S.; Xia, L.; Chen, X.; Cui, L.; Zhu, W.; Lu, Z.; Sun, J.; Fan, M. Interfacial and Electronic Band Structure Optimization for the Adsorption and Visible-Light Photocatalytic Activity of Macroscopic $ZnSnO_3$/Graphene Aerogel. *Compos. Part B Eng.* **2021**, *215*, 108765. [CrossRef]
63. Li, X.; Kang, B.; Dong, F.; Zhang, Z.; Luo, X.; Han, L.; Huang, J.; Feng, Z.; Chen, Z.; Xu, J.; et al. Enhanced Photocatalytic Degradation and H_2/H_2O_2 Production Performance of S-PCN/$WO_{2.72}$ S-Scheme Heterojunction with Appropriate Surface Oxygen Vacancies. *Nano Energy* **2021**, *81*, 105671. [CrossRef]
64. Chung, D.Y.; Uher, C.; Kanatzidis, M.G. Sb and Se Substitution in $CsBi_4Te_6$: The Semiconductors CsM_4Q_6 (M = Bi, Sb; Q = Te, Se), $Cs_2Bi_{10}Q_{15}$, and $CsBi_5Q_8$. *Chem. Mater.* **2012**, *24*, 1854–1863. [CrossRef]

65. Jiang, X.; Yu, F.; Wu, D.; Tian, L.; Zheng, L.; Chen, L.; Chen, P.; Zhang, L.; Zeng, H.; Chen, Y.; et al. Isotypic heterojunction based on Fe-doped and terephthalaldehyde-modified carbon nitride for improving photocatalytic degradation with simultaneous hydrogen production. *Chin. Chem. Lett.* **2021**, *32*, 2782–2786. [CrossRef]
66. Bai, S.; Qiu, H.; Song, M.; He, G.; Wang, F.; Liu, Y.; Guo, L. Porous fixed-bed photoreactor for boosting C–C coupling in photocatalytic CO2 reduction. *eScience* **2022**, *2*, 428–437. [CrossRef]
67. Hao, W.; Teng, F.; Liu, Z.; Yang, Z.; Liu, Z.; Gu, W. Synergistic Effect of Mott-Schottky Junction with Oxygen Defect and Dramatically Improved Charge Transfer and Separation of Bi@Bi-Doped TiO_2. *Sol. Energy Mater. Sol. Cells* **2019**, *203*, 110198. [CrossRef]